Geodynamic and climatic forcing on late-Cenozoic exhumation of the Southern Patagonian Andes (Fitz Roy and Torres del Paine massifs)

Veleda A.P. Muller[1,2], Christian Sue[2,3], Pierre G. Valla[2], Pietro Sternai[1], Thibaud Simon-Labric[2,4], Cécile Gautheron[5,2], Kurt Cuffey[6], Djordje Grujic[7], Matthias Bernet[2], Joseph Martinod[2], Matias C. Ghiglione[8], Peter Reiners[9], Chelsea Willett[6], David Shuster[6], Frédéric Herman[10], Lukas Baumgartner[11], Jean Braun[2,12,13]

[1] Dipartimento di Scienze dell'Ambiente e della Terra (DISAT), Università degli Studi di Milano-Bicocca, Piazza della Scienza 4, Milan, Italy.

[2] Institute des Sciences de la Terre (ISTerre), Université Grenoble Alpes, Université Savoie Mont Blanc, CNRS, IRD, IFSTTAR, Université Gustave Eiffel, Grenoble – Chambèry, France.

[3] Université de Franche-Comté, 25000 Besançon, France

[4] Centre de Géologie Oisans Alpes, Musée des Minéraux, 38520 Bourg-d'Oisans, France

[5] Université Paris Saclay, CNRS, GEOPS, 91405, Orsay, France.

[6] Department of Geography, Department of Earth and Planetary Science, University of California – Berkeley, USA

[7] Department of Earth and Environmental Sciences, Dalhousie University, Halifax, Canada.

[8] Instituto de Estudios Andinos "Don Pablo Groeber", Universidad de Buenos Aires, CONICET, Buenos Aires, Argentina

[9] Department of Geosciences, University of Arizona, Tucson, USA

[10] Institute of Earth Surface Dynamics (IDYST), Université de Lausanne, CH-1015 Lausanne, Switzerland

[11] Institut des Sciences de la Terre (ISTE), Université de Lausanne, CH-1015 Lausanne, Switzerland

[12] Helmholtz Centre Potsdam, GFZ German Research Centre for Geosciences, Potsdam, Germany

[13] Institute of Earth and Environmental Sciences, University of Potsdam, Potsdam, Germany

Corresponding author: Veleda Muller, v.paivamuller@campus.unimib.it

Key Points:

- Apatite and Zircon (U-Th)/He data record the opening of the asthenospheric window at latitude 49°S in the Fitz Roy massif.
- Low-temperature thermochronology data record the regional onset of Patagonian glaciations and the Plio-Pleistocene climate transition.
- Along-strike correlations of low-temperature thermochronology data enable to separate climate and tectonic forcing on rock exhumation in the Patagonian Andes.

E-mail addresses: v.paivamuller@campus.unimib.it; christian.sue@univ-grenoble-alpes.fr; pierre.valla@univ-grenoble-alpes.fr; pietro.sternai@unimib.it; thibaud.simon-labric@asso-cgo.fr; cecile.gautheron@univ-grenoble-alpes.fr; kcuffey@berkeley.edu; dgrujic@dal.ca; matthias.bernet@univ-grenoble-alpes.fr; Joseph.Martinod@univ-smb.fr; matias@gl.fcen.uba.ar; reiners@arizona.edu; Lukas.Baumgartner@unil.ch; Frederic.Herman@unil.ch; dshuster@berkeley.edu; jean.braun@gfz-potsdam.de; chelsea.d.willett@gmail.com

Abstract

Deep incised glacial valleys surrounded by high peaks form the modern topography of the Southern Patagonian Andes. Two Miocene plutonic complexes in the Andean retroarc, the cores of the Fitz Roy (49°S) and Torres del Paine (51°S) massifs, were emplaced at 16.7±0.3 Ma and 12.5±0.1 Ma, respectively. Subduction of ocean ridge segments initiated at 54°S, generating northward opening of an asthenospheric window with associated mantle upwelling and orogenic shortening since 16 Ma. Subsequently, the onset of major glaciations at 7 Ma caused drastic changes in the regional topographic evolution. To constrain the respective contributions of tectonic convergence, mantle upwelling and fluvio-glacial erosion to rock exhumation, we present inverse thermal modeling of a new dataset of zircon and apatite (U-Th)/He from the two massifs, complemented by apatite $^{4}He/^{3}He$ data for Torres del Paine. Our results show rapid rock exhumation recorded in the Fitz Roy massif between 10.5 and 9 Ma, which we ascribe to mantle upwelling and/or crustal shortening due to ridge subduction at 49°S. Both massifs record a pulse of rock exhumation between 6.5 and 4.5 Ma, which we interpret as the result of the onset of Patagonian glaciations. After a period of erosional quiescence during the Miocene/Pliocene transition, increased rock exhumation since 3-2 Ma to present day is interpreted as the result of alpine glacial valley carving promoted by reinforced glacial-interglacial cycles. This study demonstrates that along-strike thermochronological studies provide us with the means to assess the spatio-temporal variations in tectonic, mantle, and surface processes forcing on rock exhumation.

1. Introduction

Orogens that form along subduction and continental collision zones grow and evolve according to a long-term balance between incoming flux by tectonic accretion and outgoing flux by climate-driven erosion (Dahlen, 1990; Ruddiman et al., 1997; Willett, 1999; Willett et al., 2001; Beaumont et al., 2001; Egholm et al., 2009; Whipple, 2009). Compression is primarily accommodated by folds, nappes stacking, thrusts, and transpressive faults, that lead to lithospheric shortening and thickening as well as to surface uplift (Dahlen, 1990; Willett, 1999). At depths, lithospheric slab subduction and upper mantle dynamics modulate the stress and thermal states of the crust, thereby affecting rock and surface uplift (e.g., Molnar et al., 1993; Heuret and Lallemand, 2005; Conrad and Husson, 2009; Guillaume et al., 2010; Faccena et al., 2013; Sternai et al., 2019). At the surface, erosion shapes the relief of orogens, exhuming rocks and generating sediments, which subsequently fill topographic depressions, i.e., basins (England and Molnar, 1990; Whipple and Tucker, 1999; Willett, 1999; Brocklehurst, 2010; Whipple, 2009; Champagnac et al., 2014). Climate-controlled erosion and lithospheric/deep-seated processes are intrinsically linked and operate at various spatial and temporal scales, and quantifying their relative contributions to rock exhumation and landscape evolution in orogenic settings is of prime importance in current geoscience research.

85 The erosional mass outflux from glaciated orogens largely depends on the partitioning
86 between glacial processes that widen and deepen valleys (Brocklehurst and Whipple, 2006;
87 Shuster et al., 2005, 2011; Herman et al., 2011, 2018; Sternai et al., 2011, 2013), and fluvial
88 erosion, which is primarily controlled by the local slope, water discharge, and rock erodibility
89 (Willett, 1999; Whipple and Tucker, 1999; Braun and Willett, 2013). The global cooling
90 during the late Cenozoic and associated onset of glaciations generated cyclic shifts in
91 fluvial/glacial erosional processes with associated transience in mountain landscape and
92 surface uplift (Peizhen et al., 2001; Molnar, 2004; Egholm et al., 2009; Koppes and
93 Montgomery, 2009; Valla et al., 2011; Herman et al., 2013, 2018). At orogenic scale, the
94 glacier's Equilibrium Line Altitude (ELA) may limit the elevation of glaciated mountain
95 ranges, independent of the tectonic uplift rate (Montgomery et al., 2001; Egholm et al., 2009).
96 Other studies, however, suggested that tectonic uplift modulates both fluvial and glacial
97 erosion rates in orogens (Koppes and Montgomery, 2009). The impact of glacial erosion on
98 the elevation and topographic relief of mountain ranges is complex and depends on factors
99 such as bedrock physical properties, pre-glacial mountain topography, basal ice thermal
100 regime, etc. (e.g., Sternai et al., 2013; Pedersen and Egholm, 2013, and references therein).
101 The basal thermal regime of ice masses, in particular, modulates glacial erosion rates such
102 that wet and warm-based glaciers are more prone to generate glacier sliding and higher
103 erosion rates (e.g., Pedersen and Egholm, 2013), whereas dry and cold-based glaciers shield
104 the underneath bedrock from erosion, allowing topographic growth by tectonic rock uplift
105 (e.g., Thomson et al., 2010).
106 The typical steep and high topographic relief of glaciated mountain belts, with deeply
107 incised valleys, exposes lithospheric bedrock from various crustal depths. Generally,
108 crystalline rocks (i.e., magmatic and metamorphic rocks) offer a higher resistance to erosion
109 compared to soft rocks (i.e., volcano-sedimentary rocks), and tend to form prominent peaks in
110 alpine settings (Egholm et al., 2009; Shuster et al., 2011; Champagnac et al., 2014). Low-
111 temperature thermochronological bedrock ages vary systematically with elevation, low
112 elevation rocks being more recently exhumed. Age-elevation relationships, thus, allow
113 estimating regional exhumation rates (Wagner and Reimer, 1972; Wagner et al., 1979;
114 Fitzgerald and Gleadow, 1988; Fitzgerald et al., 1995; Braun, 2002; Reiners and Brandon,
115 2006) and provide useful information to unravel the exhumation history of orogenic regions
116 and the balance between regional erosion and tectonic uplift (Willett et al., 2001; Spotila,
117 2005; Tomkin and Roe, 2007; Berger et al., 2008).

In the Southern Patagonian Andes, glacial landscapes and related sedimentary deposits were proposed to reflect the onset of major glaciations in the latest Miocene (at 7 Ma; Mercer and Sutter, 1982; Zachos et al., 2001; Thomson et al., 2001, 2010; Rabassa, 2008; Lagabrielle et al., 2010; Georgieva et al., 2016, 2019; Christeleit et al., 2017; Willett et al., 2020; Ronda et al. 2022). Currently, the Northern Patagonian (46–47°S), the Southern Patagonian (SPI, 48–52°S) and the Cordillera Darwin (54°S) icefields are located along the strike of the internal domain of the orogen. Our study focuses on the eastern proximity of the SPI, where mountain peaks rise above the current glaciers' ELA, which has been oscillating between 0.5 and 2 km above sea level since the Last Glacial Maximum (~21 ka, Broecker and Denton, 1990; Davies, 2020). Miocene plutonic complexes that intrude deformed Mesozoic sedimentary rocks constitute most of these high peaks, which are surrounded by steep valleys close to the ice fields, and gentle valleys towards the eastern continental foreland (Ramírez de Arellano et al., 2012; Fosdick et al., 2013). The entire region is lying above an asthenospheric window (Fig. 1), currently originating around the Chile Triple Junction (CTJ, at 46°S) where the Nazca, Antarctic and South American plates meet (Cande and Leslie, 1986; Breitsprecher and Thorkelson, 2009). The asthenospheric window opened through subduction of spreading ocean ridge segments approximately parallel to the trench. Ocean ridge collision with the subduction trench likely generated compressive deformation and tectonic uplift in the orogen, migrating northward from an initial collision around 54°S at 16 Ma to about 49°S at 12 Ma, and 47°S at 3 Ma (Fig. 1) (Cande and Leslie, 1986; Thomson et al., 2001; Ramos, 2005; Haschke et al., 2006; Lagabrielle et al., 2010; Breitsprecher and Thorkelson, 2009; Guillaume et al., 2009, 2013; Scalabrino et al., 2010; Fosdick et al., 2013; Stevens Goddard and Fosdick, 2019; Georgieva et al., 2016, 2019). Mantle upwelling during ocean ridge subduction is expected to have generated long-wavelength dynamic surface uplift and lateral tilting of the continent, following the northward motion of the CTJ (Guillaume et al., 2009; 2013).

In this study, we present new low-temperature thermochronological datasets from two of the most emblematic massifs of the Southern Patagonia Andes: the Fitz Roy (FzR, 49°S) and Torres del Paine (TdP, 51°S) (Figs. 1-4). These two regions are located south of the CTJ, and thus may have recorded the earlier effects of northward ridge subduction and asthenospheric window opening besides those of late Cenozoic glaciation (Thomson et al., 2001; Ramos, 2005; Guillaume et al., 2009, 2013; Fosdick et al., 2013; Georgieva et al., 2016, 2019; Christeleit et al., 2017; Stevens Goddard and Fosdick, 2019; Willett et al., 2020; Ronda et al., 2022). They are also located far away from the damage areas of the Liquiñe-Ofqui and the Magallanes-Fagnano strike-slip fault zones, enabling us to dismiss any potential effect on

the regional exhumation and/or thermal impact associated to these major transcurrent structures (Thomson et al., 2001; Lagabrielle et al., 2010; Guillaume et al., 2013). Because these two massifs are located 200 km apart along the strike of the orogen, their comparative study also enables us to interpret their local and/or regional exhumation histories including transient processes. Our main goal is to decipher the partitioning between geodynamic- and climate-driven processes to rock exhumation in the Southern Patagonian Andes.

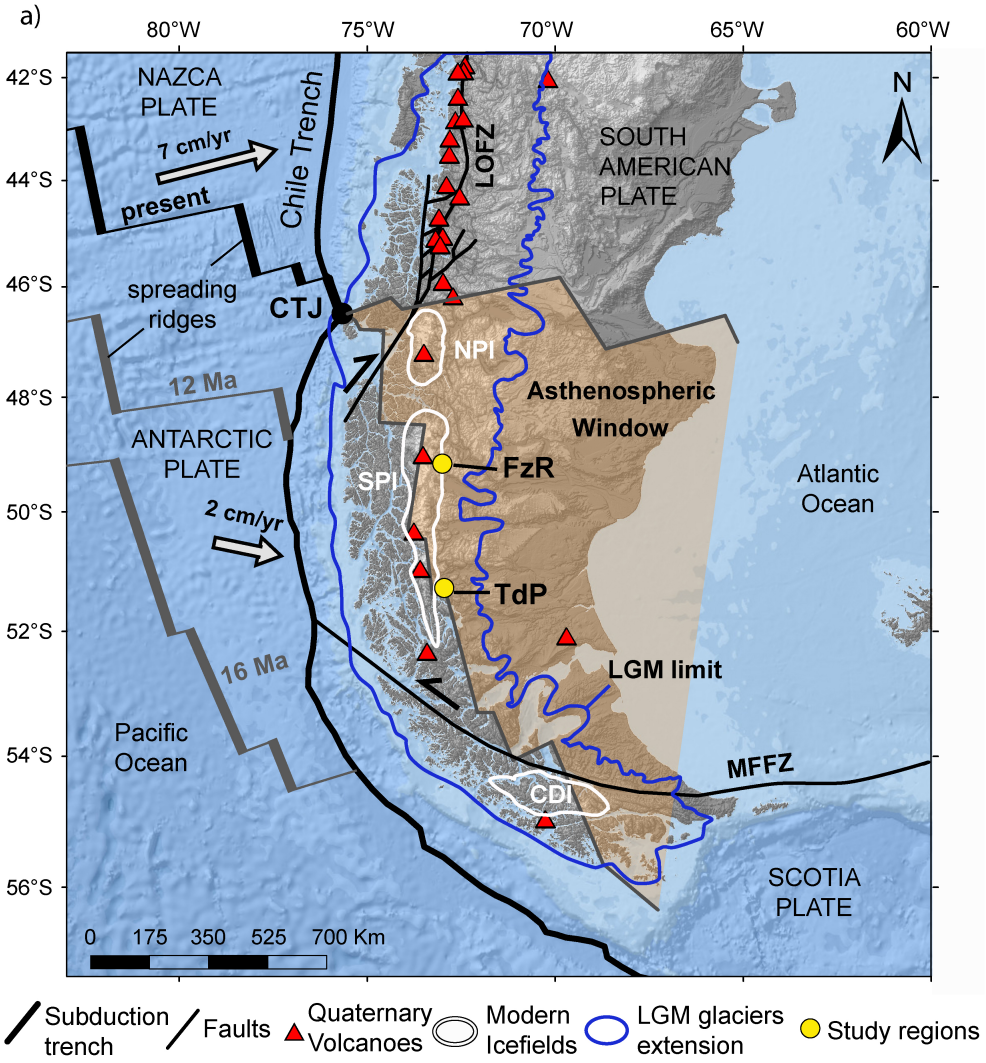

Figure 1. Geodynamic context of the Southern Patagonian Andes. The orange region represents the current asthenospheric window, the Chile Triple Junction (CTJ, black circle) is located where the ocean Chile Ridge is currently subducting beneath the South American Plate. The black and gray lines between the Nazca and the Antarctic plates are the present day, and the ancient positions (at ~16 and ~12 Ma), respectively, of the spreading ocean ridges and transform faults separating the oceanic plates (Breitsprecher and Thorkelson, 2009). The gray arrows show the velocity and approximate direction of subduction of the Nazca and Antarctic plates (DeMets et al., 2010). Red triangles show Quaternary volcanoes (Global Volcanism Program, 2023). Low-temperature thermochronometric data presented in this study are from the Torres del Paine (TdP) and Fitz Roy (FzR) massifs (yellow circles), located on the eastern border of the Southern Patagonian Icefield (SPI, white line). The blue line delimits the ice-covered region during the Last Glacial Maximum (LGM) at ~21 ka (adapted from Thorndycraft et al., 2019). Other abbreviations: NPI: Northern Patagonian Icefield, CDI: Cordillera Darwin Icefield, MFFZ: Magallanes-Fagnano Fault Zone, LOFZ: Liquiñe-Ofqui Fault Zone.

2. Geological context

2.1. Geodynamic setting

The FzR and the TdP massifs are located in the retroarc of the Southern Patagonian Andes, to the east of the N-S oriented drainage divide. Furthermore, these satellite plutons are outside of the Southern Patagonian Batholith (SPB) domain, which concentrate the locus of Late Jurassic to Miocene subduction-related magmatism intruding Paleozoic metamorphic complexes (Hervé et al., 2007). The amalgamation of the continental block bearing the SPB with the South American continent occurred in the Late Cretaceous through the closure of the ocean-floored backarc Rocas Verdes Basin (Calderón et al., 2012; Maloney et al., 2013; Muller et al., 2021). Ensuing crustal shortening and thickening in the retroarc led to foreland subsidence, and deposition of marine siliciclastic basal deposits of the Magallanes-Austral foreland basin (Fildani et al., 2003; Fosdick et al., 2011; Malkowski et al., 2017). After the break-up of the Farallon Plate into the Nazca and the Cocos plates at ~25 Ma, the increase in convergence velocity generated eastward thrust propagation into the foreland basin, forming the N-S oriented Patagonian fold-and-thrust belt (Figs. 2 and 3; Suárez et al., 2000; Kraemer, 2003; Ghiglione et al., 2009; Fosdick et al., 2011, 2013; Betka et al., 2015). Small Miocene plutonic complexes intruded the Patagonian fold-and-thrust belt, distributed for 800 km along the strike of the orogen (Ramírez de Arellano et al., 2012). In the FzR massif, the Chaltén Plutonic Complex (49°S) is composed of granitic to gabbroic rocks crystallized between 16.9±0.05 and 16.4±0.02 Ma (Ramírez de Arellano et al., 2012). Hornblende-thermobarometry from this plutonic complex indicates magmatic emplacement at 8-10 km depth and exhumation to 6-4 km depth during the syn-magmatic phase (Ramírez de Arellano, 2011). Currently, this plutonic complex is exposed, for example, in the Mount Fitz Roy (3405 m a.s.l.) and Cerro Torre (3128 m a.s.l.) (Fig. 2). The Torres del Paine Plutonic Complex, located at 51°S, is a laccolith with feeder dikes of granitic to gabbroic composition, emplaced at 2-4 km depth, as constrained from contact-metamorphic assemblages such as prehnite-anorthite (Putlitz et al., 2001), and crystallized between 12.4 ±0.006 Ma and 12.6 ±0.009 Ma (Leuthold et al., 2012). The culminant peaks of the TdP massif are the Cerro Paine Grande (2884 m a.s.l), composed of Late Cretaceous metasedimentary siliciclastic rocks encompassing the pluton, and the granitic Torre Central (2460 m a.s.l., Fig. 3).

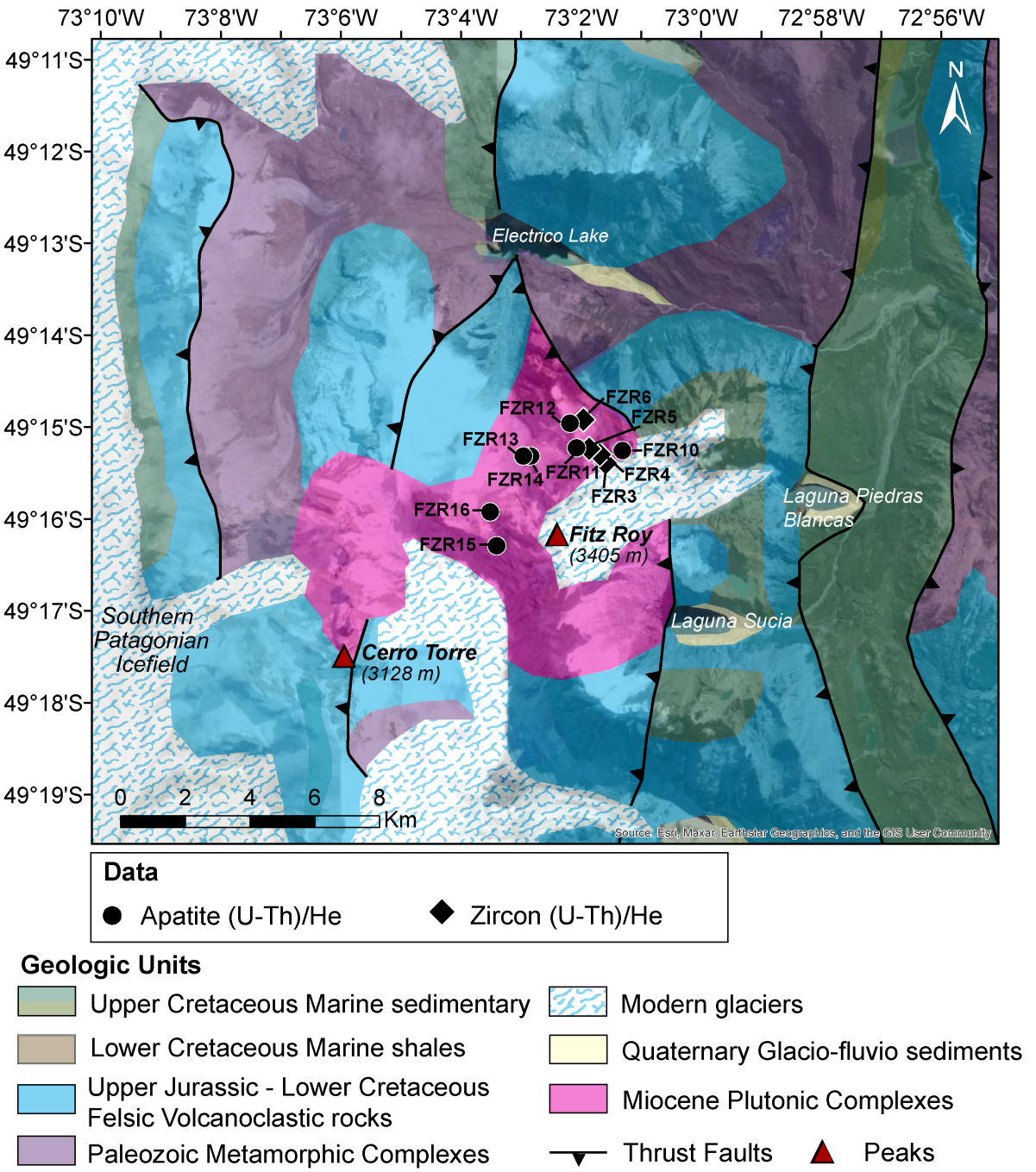

Figure 2. Geological map of the Fitz Roy massif (FzR), Argentina (modified from SEGEMAR, 2011, background satellite image is from ©Google Earth), with sample locations. Major topographic peaks are indicated by red triangles, samples for (U-Th)/He thermochronometry are located by black circles (apatite) and diamonds (zircon). See Figure 1 for location within the Southern Patagonian Andes.

The older and faster Nazca Plate subduction with respect to the Antarctic Plate generated a much longer Nazca slab than the Antarctic slab (DeMets et al., 2010; Hayes et al., 2018), with space for mantle upwelling in an asthenospheric window beneath Southern Patagonia (Fig. 1; Cande and Leslie, 1986; Ramos and Kay, 1992; Lagabrielle et al., 2004, 2007; Ramos, 2005; Breitsprecher and Thorkelson, 2009). Between 12 and 6 Ma, the

asthenospheric window broadened between latitudes 51 and 48°S, and dynamic surface uplift related to the asthenospheric flow was estimated to ~800 m (Guillaume et al., 2009). Around the current latitude of the CTJ (46-47°S) tectonic deformation and asthenospheric upwelling due to ocean ridge subduction are proposed as mechanisms forcing rock exhumation between 10 and 3 Ma (Thomson et al., 2001; Lagabrielle et al., 2004, 2007, 2010; Guillaume et al., 2009; Georgieva et al., 2016, 2019). However, its synchronicity with the onset of glaciations in Patagonia makes it difficult to separate the climate-driven from the tectonic-driven mechanisms forcing on rock exhumation (Thomson et al., 2001, 2010; Georgieva et al., 2016, 2019; Christeleit et al., 2017; Willett et al., 2020; Ronda et al. 2022). Our study region located more than 300 km south of the current CTJ offers the opportunity of analyzing a sector of the Patagonian Andes where the climate-driven and the tectonic-driven signals must not be coincident in time (Fosdick et al., 2013; Stevens Goddard and Fosdick, 2019). Magmatic effects of ridge subduction include the cessation of arc volcanism (Ramos, 2005), and extensive plateau basaltic volcanism recording the opening of the asthenospheric window (Ramos and Kay, 1992; Gorring et al., 1997; Guivel et al., 2006; Breitsprecher and Thorkelson, 2009). Amongst the six Quaternary volcanoes of the Austral Andes Volcanic Zone (Stern et al., 1984; Global Volcanism Program, 2023), the closest Lautaro (49°S) and Reclus (51°S) volcanoes are located more than 20 km away from the study regions (Fig. 1), which leads us to assume negligible thermal influence from recent volcanism on the investigated FzR and TdP massifs.

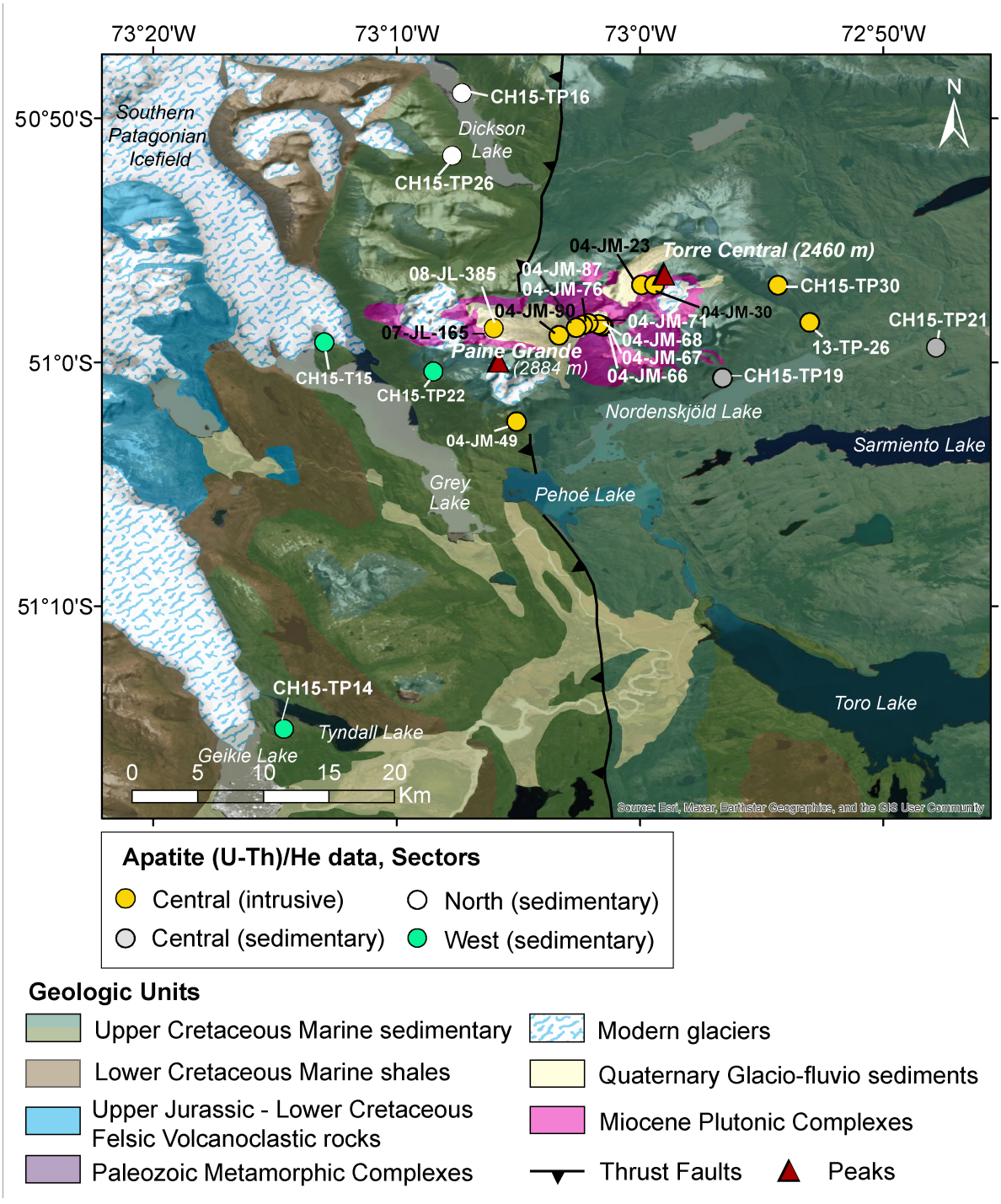

Figure 3. Geological map of the Torres del Paine massif (TdP), Chile (modified from Fosdick et al., 2013, background satellite image from ©Google Earth), with sample locations. Major topographic peaks are indicated by red triangles, samples for apatite (U-Th)/He thermochronometry are located by colored circles (see legend for details). See Figure 1 for location within the Southern Patagonian Andes.

2.2. Paleoclimatic setting and regional exhumation record

The Southern Patagonian Andes are approximately perpendicular to the main wind trend dominated by the Westerlies, thus acting as an orographic barrier since at least the early Miocene (Blisniuk et al., 2006; Fosdick et el., 2013). As a result, the precipitation rates are

higher than 4000 mm/yr on the windward side of the orogen, where the SPB is located, whereas the region located to the east of the topographic divide, including the FzR and the TdP massifs, is in a rain shadow (Blisniuk et al., 2006; Fosdick et al., 2013; Herman and Brandon, 2015). Low-temperature thermochronological ages (apatite and zircon (U-Th)/He and fission tracks) from the SPB range from 60 to 10 Ma, being generally younger eastward, and were interpreted to reflect an eastward migration of the topographic divide and exhumation front (Thomson et al., 2001; 2010). Within the Patagonian fold-and-thrust belt, including the TdP massif, recorded cooling ages range between 22 and 10 Ma ascribed to erosional exhumation during thrusting, and between 7 and 3 Ma ascribed to climate-driven exhumation mainly associated to glacio-fluvial erosion (Thomson et al., 2010; Fosdick et al., 2013; Herman and Brandon, 2015; Christeleit et al., 2017; Willett et al., 2020; Ronda et al., 2022). There are no low-temperature thermochronological ages younger than 3 Ma in the area, thus limiting our knowledge of the most recent exhumation history in the region.

The onset of Patagonian glaciations at around 7 Ma is supported by sedimentary and geomorphologic evidence, including glacial troughs, striations and moraine deposits up to 100 km eastward distant from the sediment sources (Mercer and Sutter, 1982; Zachos et al., 2001; Singer et al., 2004; Rabassa et al., 2005; 2011; Lagabrielle et al., 2010). In the CTJ region, thermochronological ages of 4–3 Ma were associated with both changing glacial/interglacial cycles, and faulting due to spreading ridge and transform faults interaction with the orogen (Thomson et al., 2001; Lagabrielle et al., 2010; Scalabrino et al., 2010; Georgieva et al., 2016; 2019; Willett et al., 2020; Ronda et al., 2022). The maximum extent of the cordilleran ice sheet (during the so-called Great Patagonian Glaciation) has been dated at ~1 Ma, and was followed by glacial episodes that reveal a gradual shrinking of the ice cover (Kaplan et al., 2004; Singer et al., 2004; Hein et al., 2011). During the Last Glacial Maximum, the region between 38 and 56 °S formed the Patagonian Ice Sheet (Fig. 1; Kaplan et al., 2004; Glasser and Jansson, 2008; Davies and Glasser, 2012; Thorndycratf et al., 2019; Davies, 2020). An orogen-scale southward increase in thermochronological ages south of 49 °S was interpreted as a decrease in the long-term erosional efficiency due to bedrock shielding by cold-based glaciers at high latitudes (Thomson et al., 2010). However, the effects of cold-based glaciers on long-term bedrock exhumation, and whether topographic relief in the Southern Patagonian Andes may surpass the glacier's ELA due to bedrock protection, are still discussed (Egholm et al., 2009; Thomson et al., 2010).

3. Materials and Methods

3.1. Sample locations and processing

Sampled bedrock outcrops are distributed within the FzR and TdP massifs, with a sampling strategy along elevation profiles when possible (Figs. 2-4). The FzR profile covers 660 m elevation (Figs. 2, 4a and 5a) over 3-4 km of horizontal distance of magmatic rocks of the Chaltén Plutonic Complex. We collected 7 samples for apatite (U-Th)/He (AHe) dating and 4 samples for zircon (U-Th)/He (ZHe) dating (Tables 1-2). In the TdP massif, AHe samples were collected from three sectors (Central, North and West, Figs. 3 and 4b,c), with 2 samples from the Central sector also having apatite $^{4}He/^{3}He$ data (Fig. 5b, Tables 3a-c and S1). The Central sector covers 1600 m elevation over 15 km of horizontal distance, while the West and North sectors extend over 630 m and 550 m elevation respectively (Figs. 3 and 4c). The Central sector is comprised of 15 magmatic samples from the Torres del Paine Plutonic Complex and 2 metasedimentary samples from the Patagonian fold-and-thrust belt located near the Nordenskjöld Lake (Figs. 3 and 4b). The West sector is comprised of 3 samples of metasedimentary rocks near the Grey and Tyndall lakes, whereas the North sector has 2 samples of metasedimentary rocks near the Dickson Lake (Figs. 3 and 4c).

Apatite and zircon crystals were extracted from bedrock samples using crushing followed by standard magnetic and heavy-liquid separation techniques (Kohn et al., 2019). For apatite, preparation included selection of crystals with euhedral shape, equivalent spherical radius between 30 and 100 μm (Tables 2 and 3), and absence of inclusion.

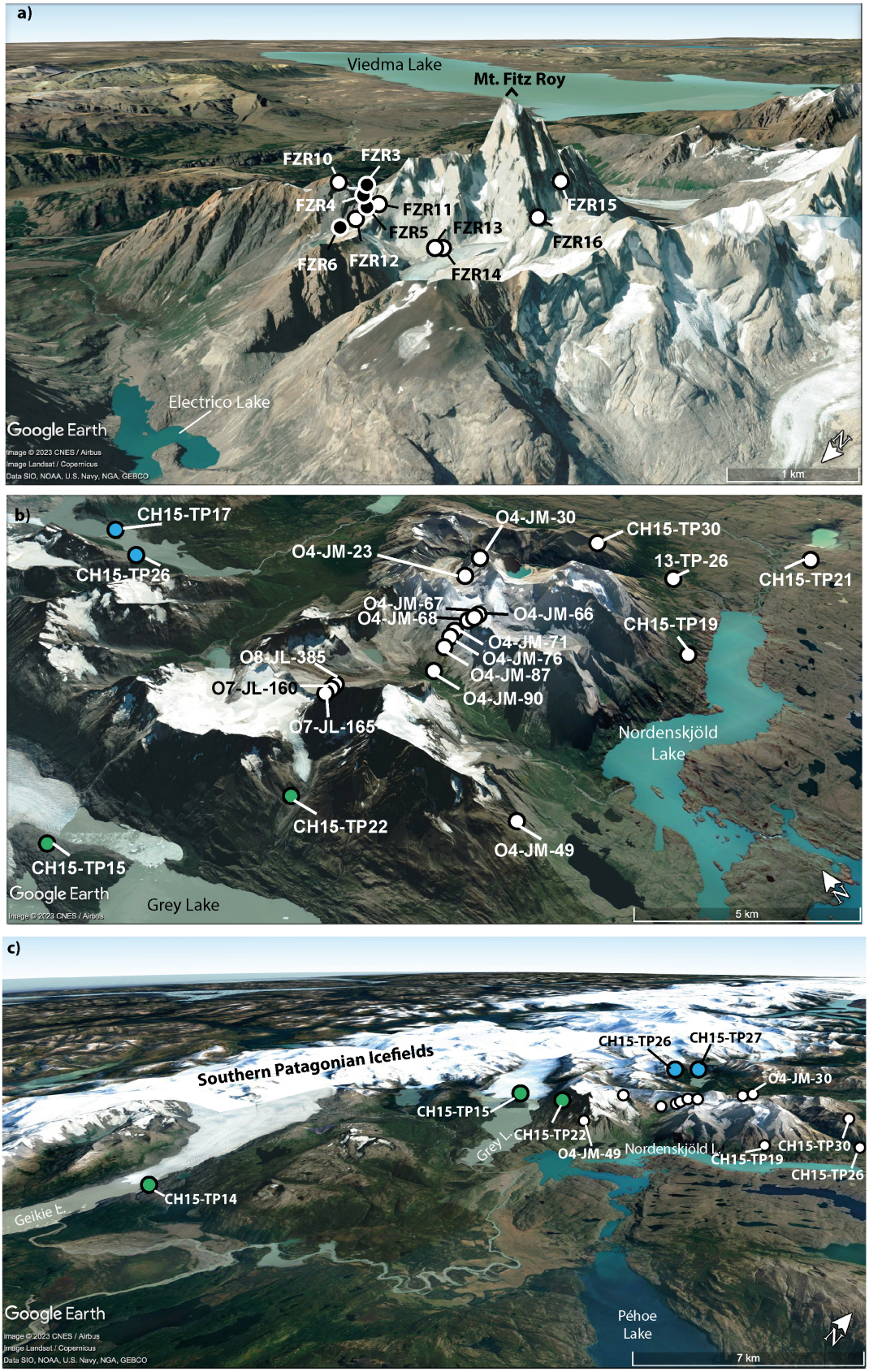

Figure 4. Samples spatial distributions within the FzR and TdP study regions. a) Fitz Roy massif and sample labels with AHe data (white circles) and ZHe data (black circles). b-c) Torres del Paine massif and sample labels with AHe data from the Central sector (white circles, b-c), and from the North (blue circles, b-c) and the West (green circles, b-c) sectors.

3.2. AHe and ZHe thermochronology data

Both methods used in this study (ZHe and AHe dating) are based on ^{4}He production and accumulation within a crystal coming from alpha radioactive decay of the parent nuclides ^{238}U, ^{235}U, ^{232}Th, and ^{147}Sm (Zeitler et al., 1987; Farley, 2002). Helium being a gas, it accumulates in a crystal depending on the diffusion coefficient, crystal size, and broken tips (e.g., Reiners and Farley, 2001; Brown et al., 2013). He diffusion in apatite and zircon is strongly controlled by radiation damage that accumulates in crystals with time (Shuster et al., 2006; Reiners, 2005). In consequence, He retention is complex and the associated effective closure temperature (T_c) and partial retention zone (PRZ) vary with damage dose production and annealing through time (Dodson, 1973). The T_c represents the temperature where 50% of the produced He atoms are retained in a crystal structure for a monotonic cooling, and the He-PRZ is the zone between 10 and 90% of the produced retained He atoms. Those notions are purely mathematic formulations but illustrate the temperature sensitivity of a thermochronological system. As a result, (U-Th)/He age varies depending on the crystal size, U and Th content (Farley, 2002; Reiners, 2005), and chemical composition for apatite (Gautheron et al., 2013). For apatite, the He-PRZ increases with damage dose from 40 to 120 °C (Shuster et al., 2006; Gautheron et al., 2009; Flowers et al., 2009; Djimbi et al., 2015). Whereas for zircon, the He-PRZ increases with radiation damage from 100 to 200 °C (Guenthner et al., 2013; Gautheron et al., 2020; Gérard et al., 2022) until a threshold and decreases up to a temperature <100 °C (Ketcham et al., 2013; Guenthner et al., 2013).

For apatite, He diffusion algorithms exist that take into account damage production and annealing, and here we used the model of Flowers et al. (2009). This model was chosen because the radiation damage present in the apatite crystal of our study is relatively low, as the plutonic rocks are young (16.7±0.3 Ma, Ramírez de Arellano et al., 2012). For zircon from the FzR plutonic complex, we used an adapted He diffusion coefficient, with He diffusion parameters calculated based on Gautheron et al. (2020), taken into account the plutonic rock age and U-Th content (Tables 1 and S2). The calculated closure temperature of the ZHe system ranges between ~87 and ~108 °C for the FzR samples (See Supplementary Material and Table S2 for details).

AHe thermochronometry was performed following standard procedures (House et al., 2000) at the ARHDL of University of Arizona (USA) for magmatic samples of TdP, and at the Berkeley Geochronology Center (USA) for metasedimentary samples of TdP and ^{4}He/^{3}He data. AHe thermochronometry of FzR magmatic samples was performed in the GEOPS

Laboratory in the Paris-Saclay University (Paris, France), and ZHe thermochronometry was performed in the UTHHE Laboratory of Dalhousie University (Halifax, Canada) following the methods of Reiners et al. (2004, 2005). Full analytical details for ZHe, AHe and $^{4}He/^{3}He$ data production are given in the Supplementary Material.

3.3. Inverse thermal modeling

We used inverse thermal modeling to interpret our new AHe and ZHe data in terms of bedrock cooling histories, and eventually to estimate the timing and spatial differences in exhumation histories between the TdP and FzR massifs. To this aim, we used the QTQt model (Gallagher, 2012), which is based on a Bayesian Markov-Chain Monte-Carlo approach to statistically explore different temperature-time (T-t) paths for multiple samples distributed along an elevation profile. For predicting ^{4}He diffusion in an apatite or zircon crystal, the model uses the raw contents of ^{238}U, ^{232}Th and ^{147}Sm, and the equivalent spherical radius calculated from crystal measurements in the laboratory (Tables 1-3). For AHe data, we used the ^{4}He diffusion kinetic parameters from the radiation damage and annealing model of Flowers et al. (2009). For ZHe data, we estimated and input the ^{4}He diffusion parameters (activation energy, E_a, and diffusion coefficient, D_0) for each individual zircon crystal to further investigate He diffusion in zircon (see Supplementary Material and Table S2 for details; Gérard et al., 2022). Then, we conducted several thermal QTQt inversions for FzR massif and TdP sectors (Central, West and North sectors, Fig. 4) with shared input modeling parameters in QTQt. First, we prescribed a geothermal gradient of 35±10 °C/km, according to the 70-90 mW/m^2 regional thermal flow predicted by Ávila and Dávila (2018). The geothermal gradient is allowed to vary with time within the 35±10 °C/km range, and no reheating was allowed due to the lack of evidence for reheating event in the study FzR and TdP regions during the late Miocene to Plio-Quaternary (Ramírez de Arellano et al., 2012). We considered an atmospheric lapse rate of 6±2 °C/km, and a present-day surface temperature of 1±1 °C to ensure model simulations reaching surface temperature for modern conditions (all sample locations have mean annual surface temperature below or around 0 °C). We also constrained the initial thermal constraints based on pluton crystallization ages, using temperature-time constraints of 275±25 °C (i.e. well hotter than respective T_c of the ZHe and AHe systems), and 16±1 Ma and 12±1 Ma for the FzR and TdP (Central sector) massifs, respectively. For the metasedimentary samples (West and North sectors of TdP massif), we did not impose any initial thermal constraint, and re-heating was not allowed

given the lack of evidence of thermal events after Early Cenozoic low-grade metamorphism during basin thrusting (Klepeis et al., 2010; Fosdick et al., 2011). For thermal inversion, QTQt's modeling is based on a linear interpolation between the highest and the lowest elevation samples to predict thermal paths randomly and shared geothermal gradients for all samples in an elevation profile (Figs. 6-8, S1-4) that best predicts observed thermochronological data in a consistent manner (Gallagher, 2012). QTQt inverse simulations were done for 10,000 iterations to ensure the robustness of the inversion results (see Supplementary Material).

Finally, we used thermal inversion modeling (Schildgen et al., 2010) to interpret $^{4}He/^{3}He$ thermochronological data in two TdP samples (Fig. 3, Table S1). To explore possible changes in ^{4}He diffusivity through time, all cooling paths ($20\text{-}30\times10^{3}$ iterations for each sample) began at 150 °C, well above the accumulation of radiation damage effects (Flowers et al., 2009) and ended after 10 Myr at the modern surface temperature. Following each specified cooling path, the model first calculated an AHe age that was compared to the measured age. If the predicted age was within 1 standard deviation (SD) of the mean measured age (Table 3), a model $^{4}He/^{3}He$ ratio evolution was calculated using the same analytical heating schedule as the sample and compared to observed ratios. This approach enables a random-search scheme to identify cooling histories that are compatible with the observations based on the computation of misfit statistics (M; mean of squared residuals weighted by the individual uncertainties in the ratio measurements; Schildgen et al., 2010); we set a misfit limit M~2, which corresponds to the 99% confidence level. Thermal histories yielding $M>4$ are excluded by the data, $2<M<4$ are marginally acceptable (yellow lines in Fig. 9b,d), and $M<2$ are good fits to the data (green lines in Fig. 9b,d).

4. Results

4.1. AHe and ZHe thermochronological data

We present all analytical details, as well as full AHe and ZHe data in Tables 1-3. For illustration, we report in Figure 5 both single-crystal and average AHe and ZHe corrected ages with 1 standard deviation of the single-crystal ages (1σ error) in age-elevation diagrams.

The FzR dataset (Fig. 5a) reveals single-crystal ZHe ages ranging from 6.1±0.4 to 12.9±0.8 Ma, and single-crystal AHe ages ranging between 3.1±0.1 and 9.7±0.6 Ma. The lack of clear age-elevation relationship for the entire elevation profile potentially indicates fast rock exhumation during the ~3 to 13 Ma period.

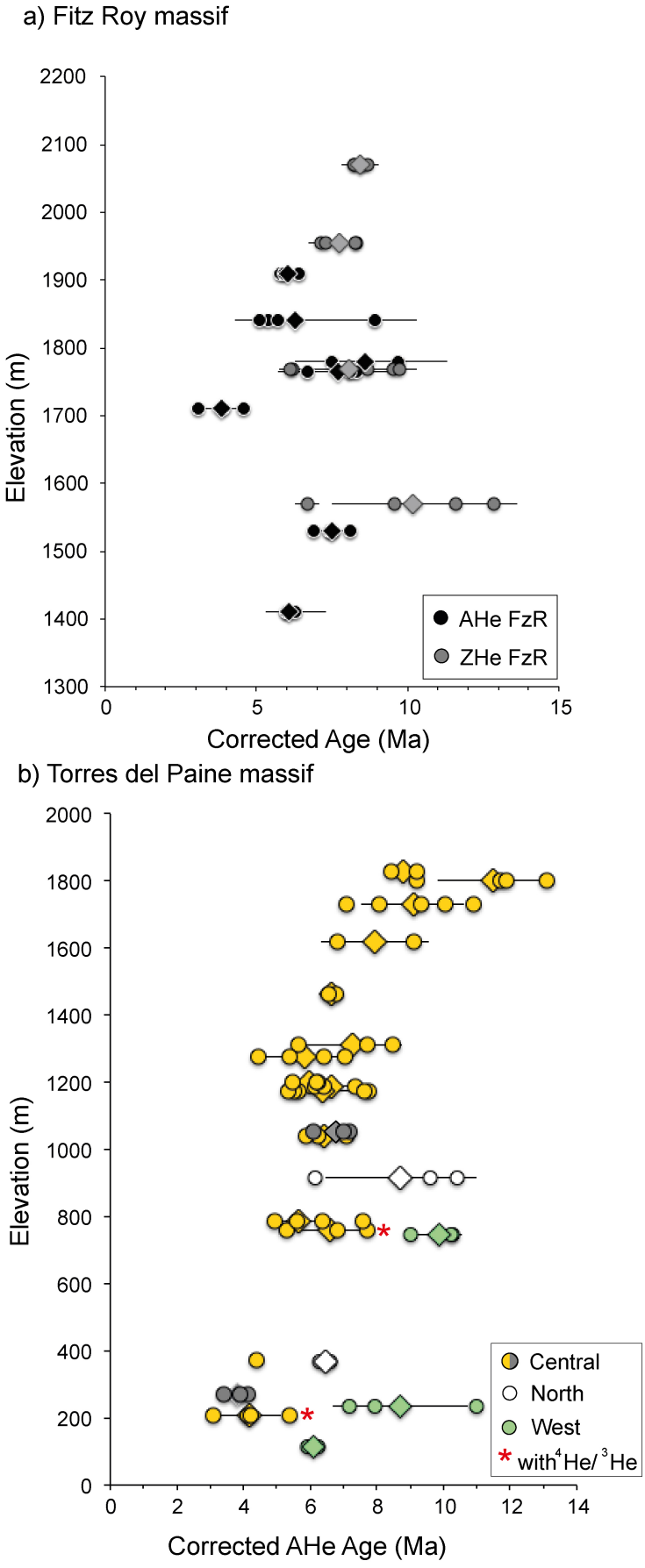

Figure 5. Age-elevation profiles for the FzR and TdP massifs. a) ZHe and AHe data for the FzR massif: single-crystal apatite and zircon (U-Th)/He ages are indicated by circles, and mean ages with 1σ errors (standard deviation of the single-crystal ages) by diamonds. b) AHe data for the TdP massif: single-crystal apatite (U-Th)/He ages are indicated by circles, and mean ages with 1σ errors (standard deviation of the single-crystal ages) by diamonds. Two samples with apatite $^{4}He/^{3}He$ data are marked by a red asterisk. Colors correspond to different sectors of the TdP massif (Central, West and North sectors), gray samples are sedimentary and yellow are magmatic samples from the Central sector, according to the legend in Figure 3, and as explained in the main text. Full analytical details for AHe and ZHe data are given in Tables 1-3 and in the Supplementary Material.

For the TdP massif, single-crystal AHe ages from the Central sector (Fig. 5b) range from 3.1±0.1 to 13.1±0.3 Ma, and the metasedimentary samples have similar ages to the magmatic samples. In addition, we observe an apparent break-in slope in the age-elevation relationship at ~7 Ma and 1400-m elevation, potentially indicating an increase in rock exhumation at this time. Samples from the North and West sectors have been collected at lower elevations (i.e. below 1000-m elevation, Fig. 5b), with AHe single-crystal ages ranging from 5.9±0.1 to 11±0.2 Ma in the West sector, and 6.3±0.2 to 10.4±0.1 Ma in the North sector.

4.2. QTQt thermal inversion results

The results of QTQt thermal inverse modeling are reported in Figures 6-8 with the relative probabilities of expected temperature-time (T-t) paths for the highest and lowest elevation samples of each elevation profile plotted in Figure 5, together with the best-fitting observed vs. predicted ages diagrams. The expected models for all the samples of each massif/sector, interpolated from the highest and the lowest elevation ones, and the output thermal gradient predicted (within the imposed range of 35±10 °C/km, see section 3.3) are shown in the Supplementary Figures S1-4. Using the output T-t paths and geothermal gradients, we can estimate exhumation rates for the different periods of time, that we have graphically determined based on major observed changes in output T-t paths (Figs. 6-8).

QTQt inversion results for the FzR massif suggest a multi-stage cooling history (Figs. 6 and S1a). Using both ZHe and AHe data, the expected (weighted mean), maximum mode, and maximum posterior thermal histories show an unconstrained cooling from the imposed initial magmatic temperature (275±25 °C) and age (16±1 Ma) constraints, to a temperature range between 110 and 70 °C at 9 Ma, showing a cooling rate of ~35 °C/Myr. At around 10.5 Ma the maximum likelihood predicted T-t paths become steeper until 9 Ma, as well as the other thermal models become steeper from 10-9.5 Ma up to 9 Ma, probably indicating an increase in the cooling rate from 35 to 60-90 °C/Ma (Fig. 6). Between 9 and 6 Ma, all the thermal models show a phase of slow cooling at 4-5 °C/Myr. At 6 Ma, both high- and low-elevation samples were rapidly cooled at ~70 °C/Myr during a short period of around 1 Myr. The highest sample (FZR3, Fig. 6a) reached surface temperatures at early Pliocene time, while the lowest elevation sample (FZR13, Fig. 6b) still experienced cooling at 5 °C/Myr with a slight increase up to 20 °C/Myr at since 1 Ma.

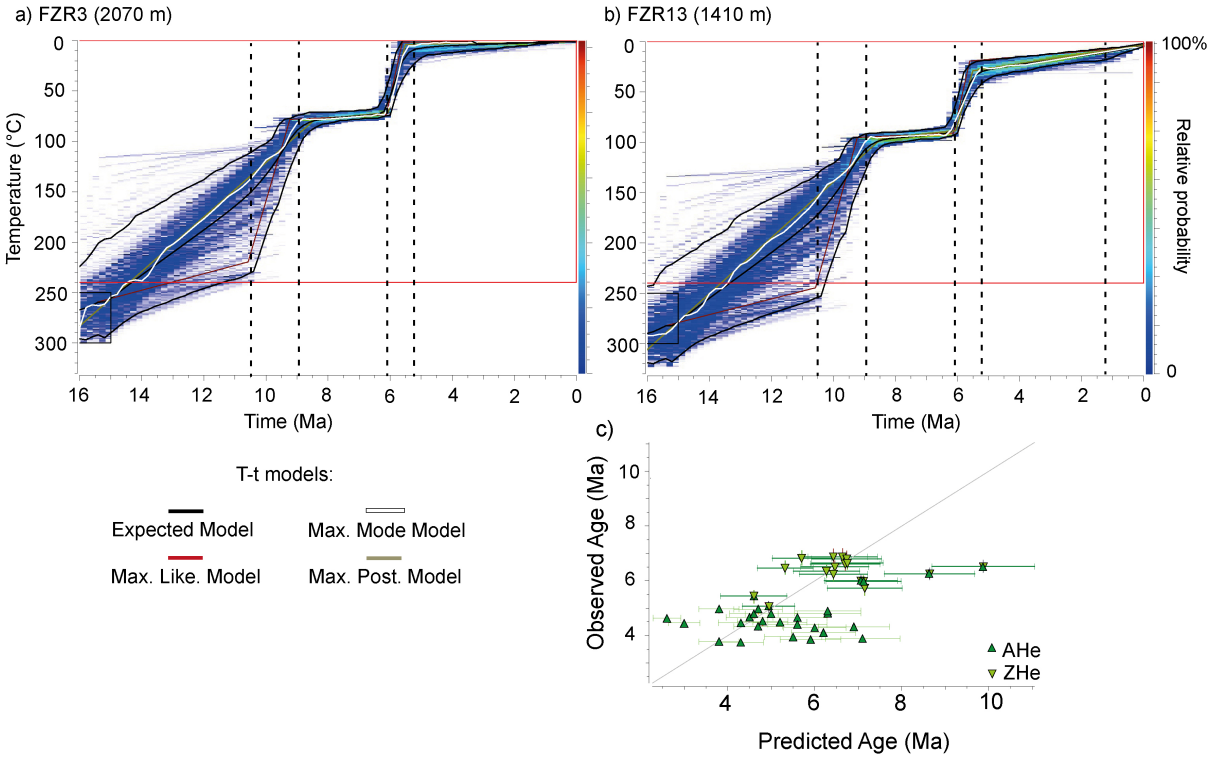

Figure 6. QTQt thermal modeling outputs for the FzR massif, derived from AHe and ZHe data (Tables 1 and 2). Selected outputs with relative probability for: a) the highest sample FZR3 (2070 m), and b) the lowest sample FZR13 (1410 m), with the expected model (weighted mean model) and its 95% confidence intervals (black solid lines), the maximum-likelihood model (red line), the maximum posterior model (green line), and the maximum mode model (white line). Black dashed lines highlight key time periods with major changes in cooling rates. The black box indicates the initial thermal constraint and the red box represents general T-t priors. Note that output thermal histories for other FzR samples are linearly interpolated between these two end members (Fig. S1). c) Best-fitting observed vs. predicted age diagram with single-crystal AHe (dark green triangles) and ZHe (downward green triangle) uncorrected ages.

For the TdP massif, inverse thermal modeling using QTQt provided variable information on the regional exhumation history from the different sectors. For the Central sector (Figs. 7 and S2), expected T-t paths from the dense AHe dataset (Fig. 5b) first show apparent rapid but unconstrained cooling from the imposed magmatic temperature/age constraints to a temperature range of 70-130 °C at around 11.5 Ma, which is the oldest thermochronological AHe age in the profile. We propose that this cooling signal has no real geological meaning since it reflects thermal adjustment after the shallow intrusion of the TdP Plutonic Complex (note that the Central sector includes also two metasedimentary samples, which we assume were re-heated by the same intrusion event). TdP samples of the Central sector then slowly cooled until 6.5 Ma, when they experienced an increase in cooling rate from <1 °C/Myr up to 90-120 °C/Myr. This fast exhumation phase was relatively short in time (during 0.5 Myr), ending at ~6 Ma, when the highest elevation sample (04-JM-66, Fig. 7a) reached almost surface temperatures. The lowest elevation sample (13-TP-26, Fig. 7b)

shows a quiescent period until 2 Ma (slow cooling at <1 °C/Myr) when it experienced an increase in cooling rate up to 30 °C/Myr. It is worth noting that the output thermal history is relatively well constrained over the late Miocene to Plio-Quaternary period because of the dense AHe dataset and well prescribed AHe age-elevation relationship (Fig. 5b).

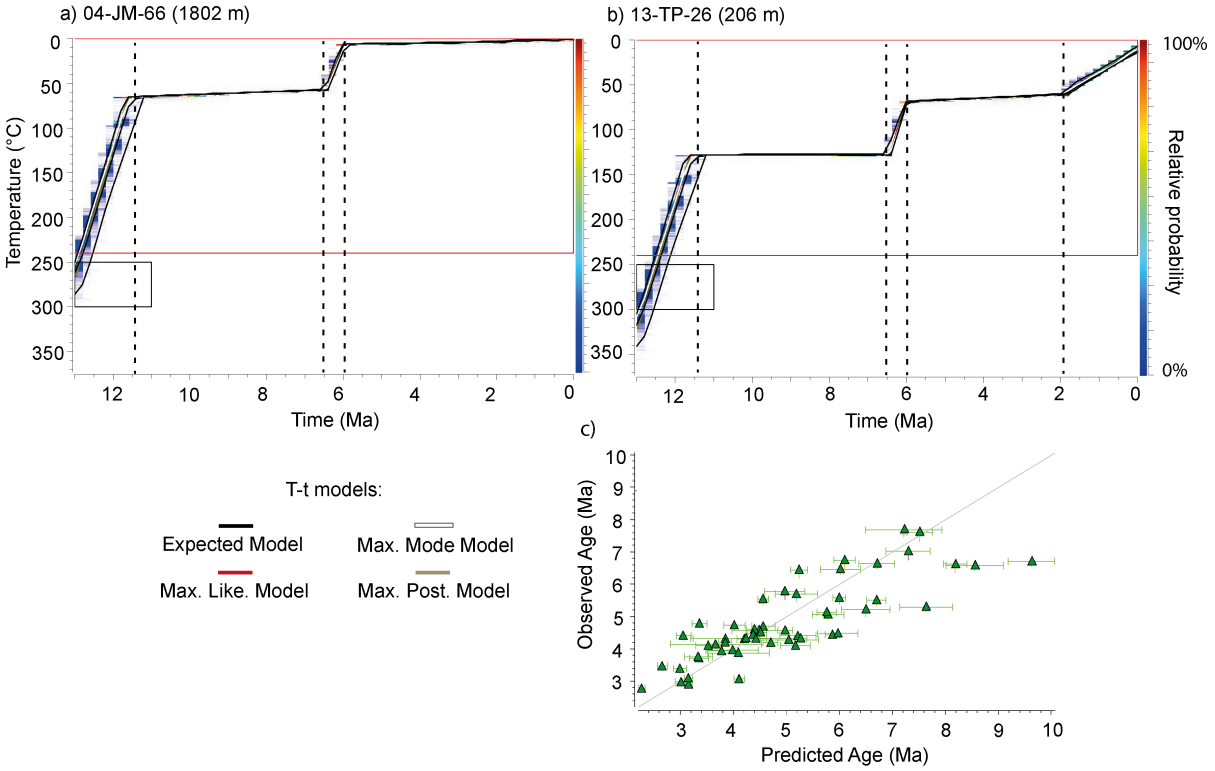

Figure 7. QTQt thermal modeling outputs for the Central sector of the TdP massif, derived from AHe data (Table 3a). Selected outputs with relative probability for: a) the highest 04-JM-66 (1802 m), and b) the lowest 13-TP-26 (206 m) elevation samples, with the expected model (weighted mean model) and its 95% confidence intervals (black solid lines), the maximum-likelihood model (red line), the maximum posterior model (green line), and the maximum mode model (white line). Black dashed lines highlight key time periods with major changes in cooling rates. The black box indicates the initial thermal constraint and the red box represents general T-t priors. Note that output thermal histories for other TdP samples are linearly interpolated between these two end members (Fig. S2). c) Best-fitting observed vs. predicted age diagram with single-crystal AHe uncorrected ages (green triangles).

For the North and West sectors of the TdP Massif (metasedimentary samples, Fig. 8), the AHe dataset is less dense and output model predictions are less constrained. For the West sector, the expected T-t paths (Fig. 8a,b) are not well constrained until 12 Ma, after this time the relative probability for the cooling histories defines a slow cooling at 4 °C/Myr. At around 6.5 Ma, cooling accelerated to 25-30 °C/Myr for a short period of 1-1.5 Myr, bringing the high-elevation sample (Fig. 8a) to near surface temperatures. After this time-interval, the low-elevation sample (Fig. 8b) was cooled slowly to the surface (at ~2 °C/Myr), with a potential late-stage exhumation increase since 0.5 Ma (with a cooling rate up to 80 °C/Myr). For the

North sector, there is no output constraint on the thermal histories until 15 Ma (Fig. 8c,d). The output thermal history reveals slow cooling between 15 and 5 Ma, with an estimated cooling rate <2 °C/Myr, followed by a short cooling episode between 5 and 4 Ma at 40-60 °C/Myr. The low-elevation sample (Fig. 8c) also recorded cooling after 4 Ma, but this phase is relatively unconstrained, although a potential acceleration in cooling rate may occur since 0.5 Ma (from 20 up to 40 °C/Ma, Fig. 8d).

Potential cooling events before 15 Ma would not have been recorded by the AHe dataset in the TdP massif. All TdP sectors show a short episode of fast cooling between 6.5 and 4 Ma, which is common between the magmatic and the metasedimentary samples, and a potential delay (or lower precision in timing) for this event north of the TdP massif (North sector). Finally, the final stage of cooling is revealed for all low-elevation samples (Figs. 7b and 8b,d), but the timing of onset for this episode appears spatially variable, being apparently earlier (at 2 Ma) for the Central sector compared to the West and North sectors (at 0.5 Ma).

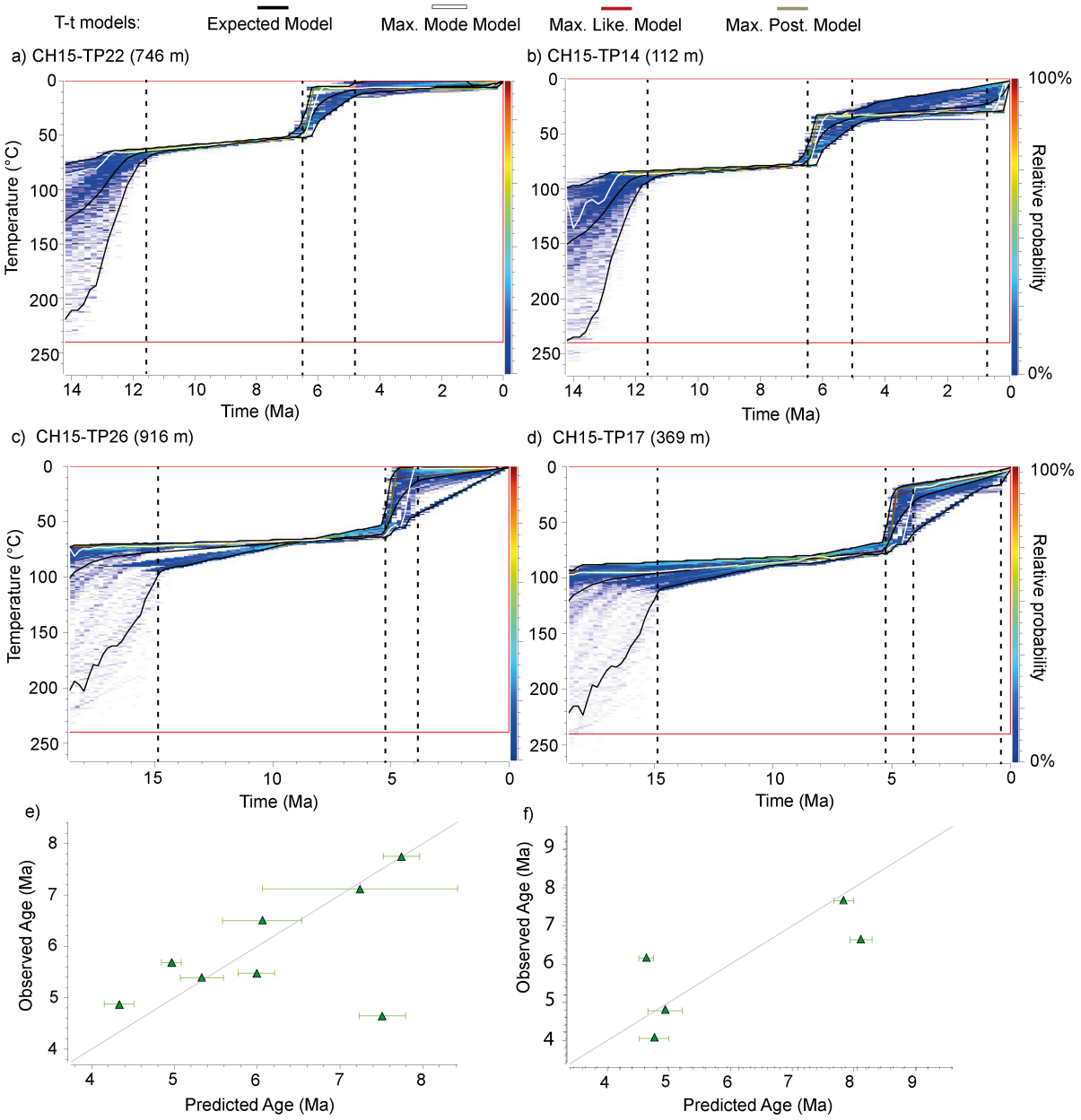

Figure 8. QTQt thermal modeling outputs for the West and North sectors of the TdP massif, derived from AHe data (Tables 3b,c). Selected outputs with relative probability for: a) the highest CH15-TP22 (746 m), and b) the lowest CH15-TP14 (112 m) elevation samples of the West sector, c) the highest CH15-26 (916 m), and the d) lowest CH15-TP17 (369 m) elevation samples of the North sector, with the expected model (weighted mean model) and its 95% confidence intervals (black solid lines), the maximum-likelihood model (red line), the maximum posterior model (green line), and the maximum mode model (white line). Black dashed lines highlight key time periods with major changes in cooling rates. The red box represents general T-t priors. Note that output thermal histories for other TdP samples are linearly interpolated between these two end members (Figs. S3 and S4). e, f) Best-fitting observed vs. predicted age diagram with single-crystal AHe uncorrected ages (green triangles) of the West and North sectors.

4.3. $^{4}He/^{3}He$ thermal histories

Inverse thermal modeling of $^{4}He/^{3}He$ data shows variable resolution for the two TdP samples (Central sector, Figs. 5b and 9). $^{4}He/^{3}He$ data resolution is relatively low for sample

13-TP-26 (Fig. 9c), resulting in unconstrained output cooling histories over the last 10 Ma. However, significant cooling (40-50 °C) had still occurred for this sample since 5-6 Ma (Fig. 9d). $^{4}He/^{3}He$ data resolution is much higher for sample 04-JM-90 (Fig. 9a) and associated output cooling histories (Fig. 9b) suggest fast cooling until 6 Ma before a quiescent period of low cooling rates. This thermal history is relatively similar to QTQt outcomes for the Central sector (Fig. 7). Finally, a late-stage cooling episode is recorded since 2 Ma, coherent with QTQt thermal predictions for the lowest elevation sample of the Central sector (Fig. 7b).

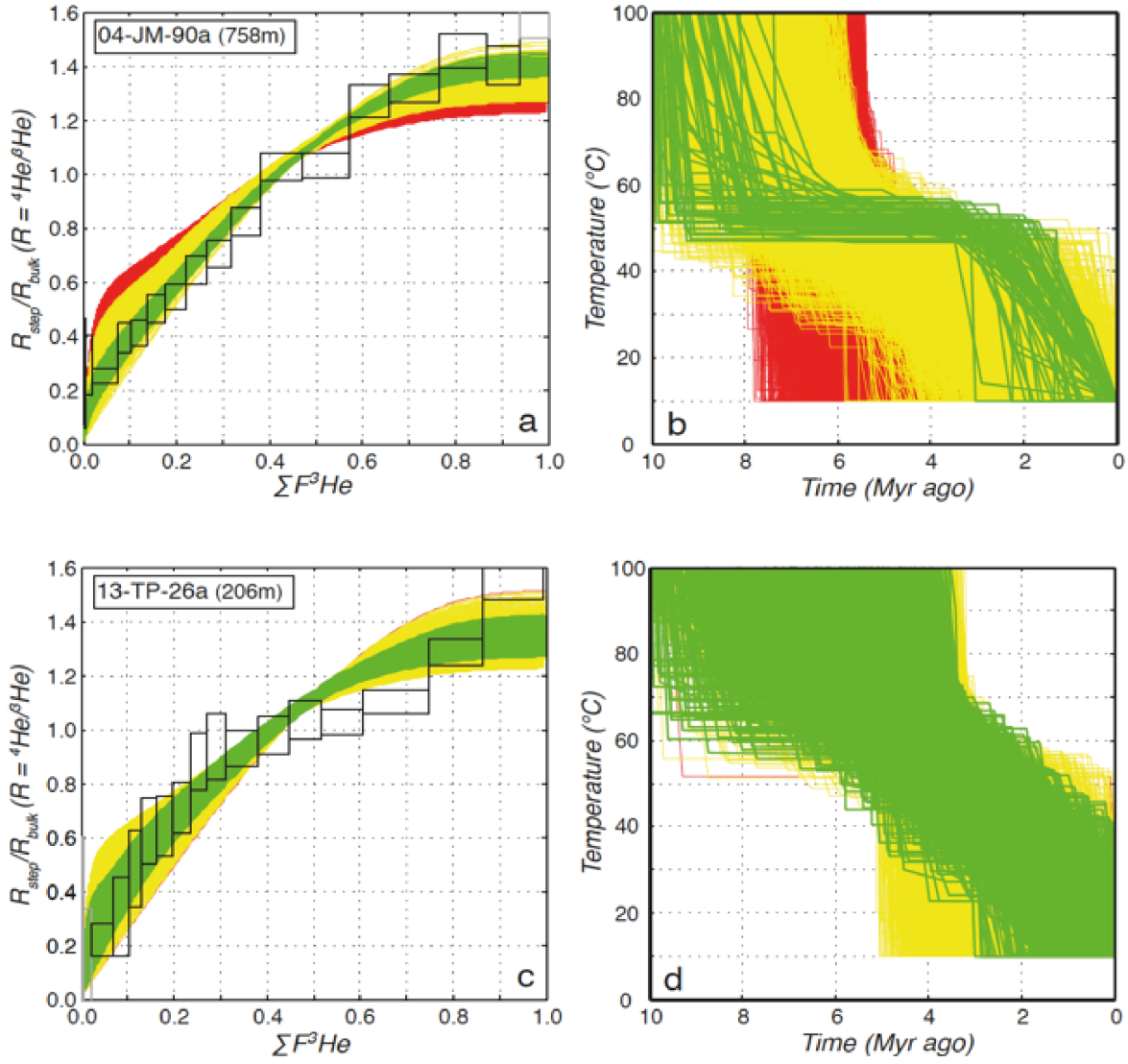

Figure 9. $^{4}He/^{3}He$ thermochronometry of TdP massif (see Figs. 3-5 for locations and details). $^{4}He/^{3}He$ ratio evolution diagrams and model cooling paths are shown for 04-JM-90a (a, b) and 13-TP-26a (c, d). The measured $^{4}He/^{3}He$ ratios of each degassing step (Rstep) are normalized to the bulk ratio (Rbulk) and plotted versus the cumulative ^{3}He release fraction ($\sum F^{3}He$). Boxes indicate ±1σ (vertical) and integration steps (horizontal). Colored lines show the predicted $^{4}He/^{3}He$ ratio evolution diagrams (a, c) for arbitrary cooling paths between 150 and 10 °C (b, d). Each colored path predicts the observed AHe age of the sample to within ±1σ (cooling paths failing to predict the AHe age are not shown); red and yellow cooling paths are excluded by the $^{4}He/^{3}He$ data, whereas green cooling paths are permitted (see section 3.3 and Supplementary material, and Supplementary Table S1 for analytical details).

5. Discussion

5.1. The role of ridge subduction and asthenospheric dynamics

In the FzR thermal models, an estimated rock exhumation rate (resulting from the output QTQt cooling rate divided by the predicted geothermal gradient given in Fig. S1) of 1 km/Myr before 9 Ma, drops to 0.2 km/Myr between 9 and 6 Ma (Fig. 6). Part of the initial fast exhumation rate can be associated to post-magmatic thermal relaxation after pluton emplacement. An apparent acceleration of rock exhumation to 2-3 km/Myr can be seen between 10.5 and 9 Ma, with the beginning of this pulse varying between the thermal models (10.5 – 9.5 Ma, Fig. 6). Spreading ridge subduction beneath the FzR massif occurred between 12 and 8 Ma (Cande and Leslie, 1986; Ramos, 2005; Lagabrielle et al., 2010; Guillaume et al., 2009b, 2013; Breitsprecher and Thorkelson, 2009), and asthenospheric upwelling during this process may have forced dynamic and thermal surface uplift (Conrad and Husson, 2009; Guillaume et al., 2010; Faccenna et a., 2013; Sternai et al., 2016). This would amplify the effects of surface erosion on rock exhumation over the incipient asthenospheric window at depth (Fig. 10a), thus accelerating the exhumation rate of the FzR massif in the time interval between 10.5 and 9 Ma. Furthermore, spreading ridge collision with the trench would have increased compression in the orogen with fold-and-thrust belt propagation towards the continent (Thomson et al., 2001; Ramos, 2005; Scalabrino et al., 2010; Guenthner et al., 2010; Lagabrielle et al., 2004, 2010; Georgieva et al., 2016, 2019; Stevens Goddard and Fosdick, 2019), a mechanism also suggested by numerical and analytical model outputs (Lallemand et al., 1992; Gerya et al., 2009; Salze et al., 2018), and may have played a role on accelerating rock exhumation in the FzR latitudes. Additionally, after the ocean ridge has subducted at 49°S, slower subduction of the Antarctic Plate with respect to the Nazca Plate may have reduced compression, uplift and rock exhumation across the orogen until the onset of the late Cenozoic glaciation (Suarez et al., 2000; Thomson et al., 2001), corresponding to the phase of erosional quiescence between 9 and 6 Ma.

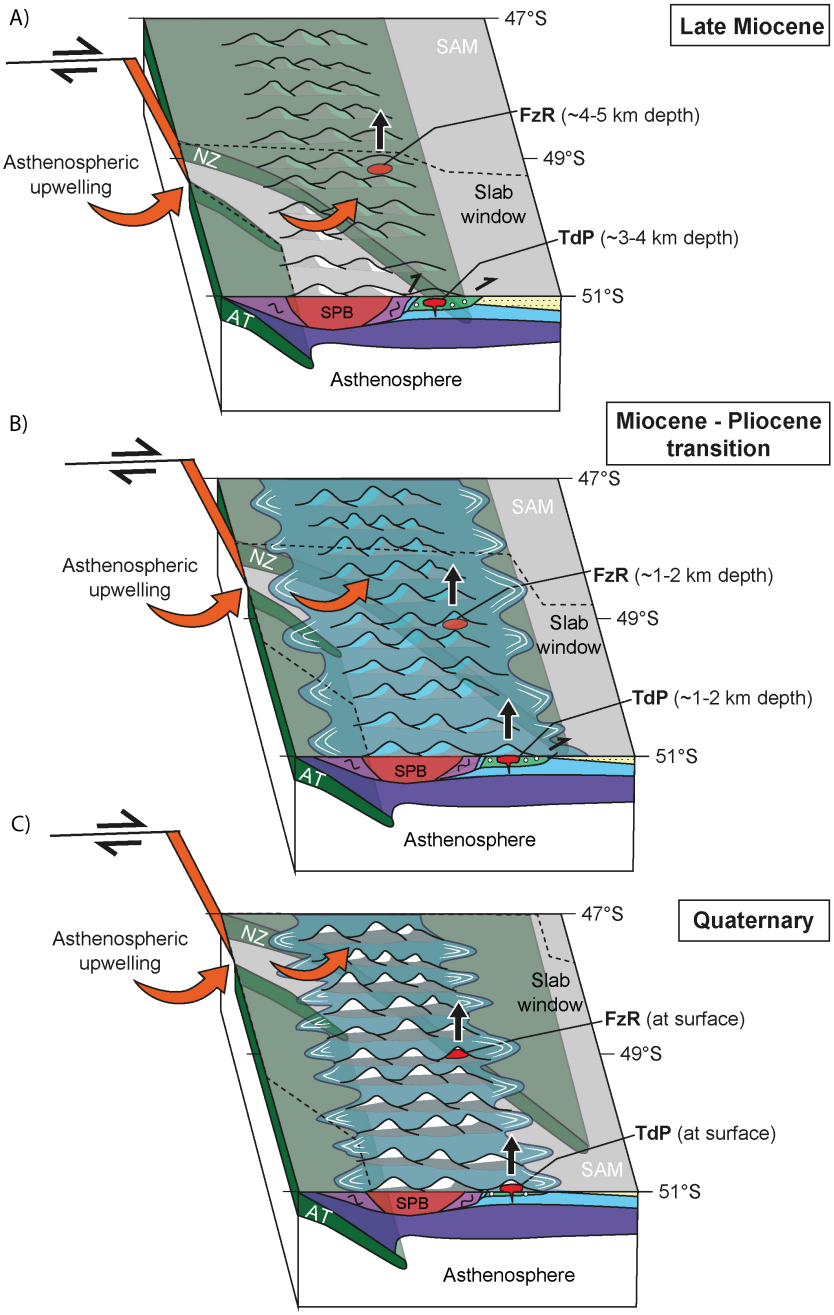

Figure 10. Block diagram with the interpretation of the geodynamic and topographic evolution of the Southern Patagonian Andes from the late Miocene to the Quaternary. a) During the late Miocene (~12 Ma), the spreading ridge between the Nazca Plate (NZ) and the Antarctic Plate (AT) was subducting beneath the South American Plate (SAM) at 49°S, asthenospheric upwelling caused dynamic and thermal surface uplift and part of the rock exhumation in the FzR massif. Deformation in the fold-and-thrust belts was active, generating crustal thickening and surface topography. The Chaltén Plutonic Complex was already emplaced at 4-5 km depth in the Fitz Roy region whereas the Torres del Paine Plutonic Complex was emplaced at 2-3 km depth. The Southern Patagonian Batholith (SPB) was already emplaced in the core of the orogen. Topography was growing by combining thrust tectonics, dynamic and thermal uplift, and erosion. b) At the Miocene – Pliocene transition (around 6 Ma), the spreading ridge was subducting at 48°S, and associated dynamic and thermal uplift should be occurring in the north of the studied regions. The Antarctic Plate was subducting at the latitudes of the studied regions and the fold-and-thrust belt and the intrusions were being exhumed mainly due to the onset of Patagonian glaciations. c) During the Quaternary, the subducting spreading ridge was at 47°S. The mountain belt was being exhumed mainly due to glacio-fluvial erosion, with carving deep valleys and leaving the mountain peaks far above the bottom of the valleys. The plutonic complexes must be at or near the surface. Black arrows highlight the uplifting regions, orange arrows highlight the region of asthenospheric upwelling.

In the TdP Massif no episode of fast cooling before the Mio-Pliocene transition appears in the thermal model outputs, but AHe ages around 12 Ma are found for high-elevation samples (Fig. 5b). These old thermochronological ages suggest that high-elevation samples were in (or near) the partial retention zone of the AHe system between 12 and 9 Ma (Figs. 5b and 7), reflecting slow exhumation at that time as confirmed by the thermal model outputs (Fig. 7). Thermochronological cooling ages between 12 and 10 Ma previously obtained in the TdP massif were also associated with thermal resetting during pluton emplacement (Fosdick et al., 2013). Dynamic surface uplift due to mantle upwelling in the region of TdP is not well constrained, and less plausible than in the FzR massif because the TdP massif is located 200 km to the south of the region where the spreading ridge has been subducting since 12 Ma (Fig. 10a).

5.2. The role of late Miocene to Plio-Quaternary glacio-fluvial erosion

The FzR and the TdP massifs share an episode of abrupt acceleration in rock exhumation between 6.5 Ma and 4.5 Ma. The onset of increased exhumation rate is synchronous with the reported stratigraphic, geomorphologic (Mercer and Sutter, 1982; Lagabrielle et al., 2004, 2007, 2009, 2010; Rabassa et al., 2005, 2011; Rabassa, 2008), and thermochronological (Thomson et al., 2001; Glodny et al., 2008; Thomson et al., 2010; Fosdick et al., 2013; Georgieva et al., 2016; 2019; Christeleit et al., 2017; Willett et al., 2020; Ronda et al., 2022) evidence for the onset of major glaciations at 7-6 Ma in the Southern Patagonian Andes. The Andean topography, therefore, quickly responded to the transition from fluvial-dominated to glacial-dominated erosional processes (Fig. 10b), as proposed for other alpine environments (Egholm et al., 2009; Shuster et al., 2005; 2011; Valla et al., 2011; Herman et al., 2013; Champagnac et al., 2014). The magnitude and duration of this event depend on the analysed sector of the TdP and FzR massifs, varying between 0.6 and 3 km/Myr. The limited exhumation in the North and West sectors of the TdP massif compared to the Central sector (Figs. 7 and 8) could reflect already existing high topographic reliefs in the North and West sectors and/or selective glacial erosion with potential glacial bedrock shielding closer to the present-day/past icefield (Rabassa, 2008, Lagabrielle et al., 2010). Efficient erosion of high-elevation topography by glacial and periglacial processes during the late Miocene would have resulted in a net decrease of ice accumulation area and hence in ice extent, ice flux, and consequently in glacial erosion (Pedersen and Egholm 2013; Sternai et al., 2013). Such negative feedback has also been proposed to explain the late Quaternary

611 gradual shrinking of the Southern Patagonian Icefield (Fig. 10c; Kaplan et al., 2009), and
612 likely explains the short-lived erosion pulse that our results and previous studies identified in
613 Southern Patagonia at the late Miocene/Pliocene transition (Christeleit et al., 2017; Willet et
614 al., 2020).
615 Pliocene low exhumation rates (<0.1 km/Myr) recorded in the FzR and TdP massifs
616 indicates erosional quiescence following high but transient glacial erosion rates in the
617 Southern Patagonian Andes (Christeleit et al., 2017; Willet et al., 2020). The late-stage
618 Quaternary fast exhumation is mainly recorded for low-elevation samples and in $^{4}He/^{3}He$
619 thermochronological data, with predicted onset varying between 2 and 0.5 Ma depending on
620 the sample location (Figs. 6-9, and S1-4). An increase in exhumation rates for several
621 mountainous regions worldwide since around 2 Ma (Herman et al., 2013) has been associated
622 with the onset of enhanced glaciations at mid latitudes, including Fjordland in New Zealand
623 (Shuster et al., 2011), Alaska (Berger et al., 2008), British Columbia (Shuster et al., 2005),
624 and the European Alps (Haeuselmann et al., 2007; Valla et al., 2011; Glotzbach et al., 2011;
625 Fox et al., 2015; 2016). A possible climatic trigger might be the observed increase in the
626 duration and asymmetry of glacial-interglacial cycles at ~1.2 Ma (Lisiecki and Raymo, 2007;
627 Lisiecki, 2010). By periodically switching between glacial and fluvial conditions, and by
628 changing associated vegetation and soil cover, geomorphic processes would remain transient
629 (Molnar, 2004; Herman and Champagnac, 2016), maintaining landscape disequilibrium and
630 in turn enhancing erosion rates (Egholm et al., 2009; Champagnac et al., 2014). North of the
631 studied region (46-47°S), stratigraphic records from moraine deposits indicate a shift in the
632 drainage network after 3 Ma, resulting in a major landscape change from a smooth piedmont
633 surface with extensive icefields in the foreland, to long west-east oriented and channelized
634 glacial lobes (Lagabrielle et al., 2010). Tectonic uplift of the eastern Patagonian foreland
635 could therefore have conditioned or at least favored such geomorphological shift and induced
636 west-east incision of deep glacial valleys, but it is mostly associated to regions to the north of
637 47°S where the interactions of the ocean ridge with the trench via compression, transpression
638 and mantle upwelling play a recent (<3 Ma) role (Lagabrielle et al., 2010; Georgieva et al.,
639 2019). In our study region (49-51°S), the recent acceleration in exhumation is most likely
640 associated with the Plio-Quaternary shift in glacial-interglacial cyclicity, enhanced glacial
641 erosional processes, and icefield drainage reorganization in Southern Patagonia (Fig. 10c).
642
643

6. Conclusions

The Southern Patagonian Andes recorded a long history of interactions between tectonics and climate-driven erosion processes. The North-South orientation of the Andean mountain belt allowed us to investigate spatial and temporal variations of these interactions. We found thermochronological evidence for the effects of ocean ridge subduction and asthenospheric upwelling to the surface uplift and rock exhumation in the Fitz Roy massif during the late Miocene (between 10.5 and 9 Ma). This event accounts for more than 2 km of rock exhumation over the late Miocene, resulting in dynamic and thermal surface uplift and/or continental compression, which increased erosion at 49°S latitude. This event was not recorded by low-temperature thermochronological data from the Torres del Paine massif, possibly due to the already attenuated surface response to ridge collision and mantle upwelling at 51°S, when the TdP pluton was emplaced at around 12.5±0.1 Ma.

The onset of glaciations in Southern Patagonia generated a regional signal of rapid rock exhumation in the Fitz Roy and Torres del Paine massifs (at 49-51°S) between 6.5 and 4.5 Ma. This was followed by a period of slow rock exhumation from the early Pliocene to the Quaternary, highlighting erosional quiescence and possibly reflecting bedrock shielding by extensive icefields covering the Southern Patagonian Andes. A late-stage Quaternary episode of accelerated rock exhumation is recorded in our thermochronological datasets, and coincides with worldwide increased mountain erosion ascribed to intense glacial-interglacial cycles. This climatic transition generated a geomorphological shift from smooth landforms to deep incised glacial valleys, leaving the high elevations of the Torres del Paine and the Fitz Roy plutonic complexes standing far above nearby valley bottoms.

7. Acknowledgments

This work has also been supported by the Italian Ministry of Education, MIUR (Project Dipartimenti di Eccellenza 2023-2027, TECLA, Department of Earth and Environmental Sciences, University of Milano-Bicocca). The Université Grenoble Alpes, the French CNRS, the INSU SYSTER project, and the ECOS-SUD project A15U02 also supported this work. V.A.P.M. acknowledges the ERASMUS+ program for the mobility grant to visit the Université Grenoble Alpes, and the TRB team. P.G.V. acknowledges funding support from the Swiss National Science Foundation SNSF (Grant PP00P2_170559) and the French ANR-PIA program (ANR-18-MPGA-0006). For permission to work and

sample in P.N. Torres del Paine, K.C. is grateful to two Chilean agencies: Corporación Nacional Forestal (Resolución 15/2015), and Dirección Nacional de Fronteras y Límites del Estado. In the P.N. Los Glaciares (Fitz Roy massif), C.S., and M.C.G. are greatful to the Administración de Parques Nacionales Argentina (permit 31-DRPA to M.C.G.), and all the people who helped us on the field, specially the mountain guide Santiago Arias in El Calafate, Argentina. We acknowledge the support of The Martin Family Foundation to K.C., The Ann and Gordon Getty Foundation to D.S., and the Chilean Comisión Nacional de Investigación Cientifica y Tecnológica award to U.C. Berkeley. M. Salze and R. Pinna-Jamme are warmly thanked for the help during AHe analysis at GEOPS.

References

Ávila, P., & Dávila, F. M. (2018). Heat flow and lithospheric thickness analysis in the Patagonian asthenospheric windows, southern South America. *Tectonophysics*, *747*, 99-107.

Berger, A. L., Gulick, S. P., Spotila, J. A., Upton, P., Jaeger, J. M., Chapman, J. B., Worthington, L.A., Pavlis, T.L., Ridgway, K.D., Willems, B.A., & McAleer, R. J. (2008). Quaternary tectonic response to intensified glacial erosion in an orogenic wedge. *Nature Geoscience*, *1*(11), 793-799.

Beaumont, C., Jamieson, R. A., Nguyen, M. H., & Lee, B. (2001). Himalayan tectonics explained by extrusion of a low-viscosity crustal channel coupled to focused surface denudation. *Nature*, *414*(6865), 738-742.

Betka, P., Klepeis, K., & Mosher, S. (2015). Along-strike variation in crustal shortening and kinematic evolution of the base of a retroarc fold-and-thrust belt: Magallanes, Chile 53° S–54° S. *GSA Bulletin*, *127*(7-8), 1108-1134.

Blisniuk, P. M., Stern, L. A., Chamberlain, C. P., Zeitler, P. K., Ramos, V. A., Sobel, E. R., Haschke, M., Strecker, M.R., & Warkus, F. (2006). Links between mountain uplift, climate, and surface processes in the southern Patagonian Andes. In *The Andes* (pp. 429-440). Springer, Berlin, Heidelberg.

Braun, J. (2002). Quantifying the effect of recent relief changes on age–elevation relationships. *Earth and Planet. Sci. Letters*, *200*(3-4), 331-343.

Braun, J., & Willett, S. D. (2013). A very efficient O (n), implicit and parallel method to solve the stream power equation governing fluvial incision and landscape evolution. *Geomorphology*, *180*, 170-179.

Breitsprecher, K., & Thorkelson, D. J. (2009). Neogene kinematic history of Nazca–Antarctic–Phoenix slab windows beneath Patagonia and the Antarctic Peninsula. *Tectonophysics*, *464*(1-4), 10-20.

Brocklehurst, S. H. (2010). Tectonics and geomorphology. *Progress in Physical Geography*, *34*(3), 357-383.

Brocklehurst, S. H., & Whipple, K. X. (2006). Assessing the relative efficiency of fluvial and glacial erosion through simulation of fluvial landscapes. *Geomorphology*, *75*(3-4), 283-299.

Broecker, W. S., & Denton, G. H. (1990). The role of ocean-atmosphere reorganizations in glacial cycles. *Quaternary Science Reviews*, *9*(4), 305-341.

Brown, R.W., Beucher, R., Roper, S., Persano, C., Stuart, F. & Fitzgerald, P. (2013) Natural age dispersion arising from the analysis of broken crystals, Part I. Theoretical basis and implications for the apatite (U-Th)/He thermochronometer. *Geochim. Cosmochim. Acta* 122, 478-497.

Calderón, M., Fosdick, J. C., Warren, C., Massonne, H. J., Fanning, C. M., Cury, L. F., Schwanethal, J., Fonseca, P.E., Galaz, G., & Herve, F. (2012). The low-grade Canal de las Montañas Shear Zone and its role in the tectonic emplacement of the Sarmiento Ophiolitic Complex and Late Cretaceous Patagonian Andes orogeny, Chile. *Tectonophysics*, *524*, 165-185.

Cande, S. C., & Leslie, R. B. (1986). Late Cenozoic tectonics of the southern Chile trench. *Journal of Geophysical Research: Solid Earth*, *91*(B1), 471-496.

Champagnac, J. D., Valla, P. G., & Herman, F. (2014). Late-Cenozoic relief evolution under evolving climate: A review. *Tectonophysics*, *614*, 44-65.

Christeleit, E. C., Brandon, M. T., & Shuster, D. L. (2017). Miocene development of alpine glacial relief in the Patagonian Andes, as revealed by low-temperature thermochronometry. *Earth and Planetary Science Letters*, *460*, 152-163.

Conrad, C. P., & Husson, L. (2009). Influence of dynamic topography on sea level and its rate of change. *Lithosphere*, *1*(2), 110-120.

Dahlen, F. A. (1990). Critical taper model of fold-and-thrust belts and accretionary wedges. *Annual Review of Earth and Planetary Sciences*, *18*, 55.

Davies, B. J., & Glasser, N. F. (2012). Accelerating shrinkage of Patagonian glaciers from the Little Ice Age (~ AD 1870) to 2011. *Journal of Glaciology*, *58*(212), 1063-1084.

Davies, B. J., Darvill, C. M., Lovell, H., Bendle, J. M., Dowdeswell, J. A., Fabel, D., García, J.-L., Geiger, A., Glasser, N.F., Gheorghiu, D.M., Harrison, S., Hein, A. S., Kaplan, M. R., Martin, J.R.V., Mendelova, M., Palmer, A., Pelto, M., Rodés, A., Sagredo, E.A., Smedley, R.K., & Thorndycraft, V. R. (2020). The evolution of the Patagonian Ice Sheet from 35 ka to the present day (PATICE). *Earth-Science Reviews*, *204*, 103152.

DeMets, C., Gordon, R. G., & Argus, D. F. (2010). Geologically current plate motions. *Geophysical journal international*, *181*(1), 1-80.

Djimbi, D.M., Gautheron, C., Roques, J., Tassan-Got, L., Gerin, C. & Simoni, E. (2015) Impact of apatite chemical composition on (U-Th)/He thermochronometry: an atomistic point of view. *Geochim. et Cosmochim. Acta* 167, 162-176.

Dodson, M. H. (1973). Closure temperature in cooling geochronological and petrological systems. *Contributions to Mineralogy and Petrology*, *40*(3), 259-274.

Dodson, M. H. (1979). Theory of cooling ages. In *Lectures in isotope geology* (pp. 194-202). Springer, Berlin, Heidelberg.

Egholm, D. L., Nielsen, S. B., Pedersen, V. K., & Lesemann, J. E. (2009). Glacial effects limiting mountain height. *Nature*, *460*(7257), 884-887.

England, P., & Molnar, P. (1990). Surface uplift, uplift of rocks, and exhumation of rocks. *Geology*, *18*(12), 1173-1177.

Evans, N. J., Byrne, J. P., Keegan, J. T., & Dotter, L. E. (2005). Determination of uranium and thorium in zircon, apatite, and fluorite: Application to laser (U-Th)/He thermochronology. *Journal of Analytical Chemistry*, *60*(12), 1159-1165.

Faccenna, C., Becker, T. W., Conrad, C. P., & Husson, L. (2013). Mountain building and mantle dynamics. *Tectonics*, *32*(1), 80-93.

Farley, K. A. (2002). (U-Th)/He dating: Techniques, calibrations, and applications. *Reviews in mineralogy and geochemistry*, *47*(1), 819-844.

Farley, K. A., Wolf, R. A., & Silver, L. T. (1996). The effects of long alpha-stopping distances on (U-Th)/He ages. *Geochimica et cosmochimica acta*, *60*(21), 4223-4229.

Fildani, A., Cope, T. D., Graham, S. A., & Wooden, J. L. (2003). Initiation of the Magallanes foreland basin: Timing of the southernmost Patagonian Andes orogeny revised by detrital zircon provenance analysis. *Geology*, *31*(12), 1081-1084.

Fitzgerald, P. G., & Gleadow, A. J. (1988). Fission-track geochronology, tectonics and structure of the Transantarctic Mountains in northern Victoria Land, Antarctica. *Chemical Geology: Isotope Geoscience section*, *73*(2), 169-198.

Fitzgerald, P. G., Sorkhabi, R. B., Redfield, T. F., & Stump, E. (1995). Uplift and denudation of the central Alaska Range: A case study in the use of apatite fission track thermochronology to determine absolute uplift parameters. *Journal of Geophysical Research: Solid Earth*, *100*(B10), 20175-20191.

Flowers, R. M., Ketcham, R. A., Shuster, D. L., & Farley, K. A. (2009). Apatite (U–Th)/He thermochronometry using a radiation damage accumulation and annealing model. *Geochimica et Cosmochimica acta*, *73*(8), 2347-2365.

Fosdick, J. C., Grove, M., Hourigan, J. K., & Calderon, M. (2013). Retroarc deformation and exhumation near the end of the Andes, southern Patagonia. *Earth and Planetary Science Letters*, *361*, 504-517.

Fosdick, J. C., Romans, B. W., Fildani, A., Bernhardt, A., Calderón, M., & Graham, S. A. (2011). Kinematic evolution of the Patagonian retroarc fold-and-thrust belt and Magallanes foreland basin, Chile and Argentina, 51 30′ S. *Bulletin*, *123*(9-10), 1679-1698.

Fox, M., Herman, F., Kissling, E., & Willett, S. D. (2015). Rapid exhumation in the Western Alps driven by slab detachment and glacial erosion. *Geology*, *43*(5), 379-382.

Fox, M., Herman, F., Willett, S. D., & Schmid, S. M. (2016). The exhumation history of the European Alps inferred from linear inversion of thermochronometric data. *American Journal of Science*, *316*(6), 505-541.

Gallagher, K. (2012). Transdimensional inverse thermal history modeling for quantitative thermochronology. *Journal of Geophysical Research: Solid Earth*, *117*(B2).

Gautheron, C., Barbarand, J., Ketcham, R., Tassan-Got, L., van der Beek, P.A., Pagel, M., Pinna-Jamme, R., Couffignal, F. & Fialin, M. (2013) Chemical influence on α-recoil damage annealing in apatite: implications for (U-Th)/He dating. *Chem. Geol.* 351, 257-267.

Gautheron, C., Djimbi, D. M., Roques, J., Balout, H., Ketcham, R. A., Simoni, E., Pik, R., Seydoux-Guillaume, A.-M., & Tassan-Got, L. (2020). A multi-method, multi-scale theoretical study of He and Ne diffusion in zircon. *Geochimica et Cosmochimica Acta*, *268*, 348-367.

Gautheron, C., Hueck, M., Ternois, S., Heller, B., Schwartz, S., Sarda, P., & Tassan-Got, L. (2022). Investigating the Shallow to Mid-Depth (> 100–300° C) Continental Crust Evolution with (U-Th)/He Thermochronology: A Review. *Minerals*, *12*(5), 563.

Gautheron, C., Pinna Jamme, R., Derycke, A., Ahadi, F., Sanchez, C., Haurine, F., Monvoisin, G., Barbosa, D., Delpech, G., Maltese, J., Sarda, P. & Tassan-Got, L. (2021). Technical note: Analytical protocols and performance for apatite and zircon (U–Th)/He analysis on quadrupole and magnetic sector mass spectrometer systems between 2007 and 2020. *Geochronology* 3, 351-370.

Gautheron, C., Tassan-Got, L., Barbarand, J., & Pagel, M. (2009). Effect of alpha-damage annealing on apatite (U–Th)/He thermochronology. *Chemical Geology*, *266*(3-4), 157-170.

Georgieva, V., Gallagher, K., Sobczyk, A., Sobel, E. R., Schildgen, T. F., Ehlers, T. A., & Strecker, M. R. (2019). Effects of slab-window, alkaline volcanism, and glaciation on thermochronometer cooling histories, Patagonian Andes. *Earth and Planetary Science Letters*, *511*, 164-176.

Georgieva, V., Melnick, D., Schildgen, T. F., Ehlers, T. A., Lagabrielle, Y., Enkelmann, E., & Strecker, M. R. (2016). Tectonic control on rock uplift, exhumation, and topography above an oceanic ridge collision: Southern Patagonian Andes (47 S), Chile. *Tectonics*, *35*(6), 1317-1341.

Gérard, B., Robert, X., Grujic, D., Gautheron, C., Audin, L., Bernet, M., & Balvay, M. (2022). Zircon (U-Th)/He closure temperature lower than apatite thermochronometric systems: reconciliation of a paradox. *Minerals*, *12*(2), 145.

Gerya, T. V., Fossati, D., Cantieni, C., & Seward, D. (2009). Dynamic effects of aseismic ridge subduction: numerical modelling. *European Journal of Mineralogy*, *21*(3), 649-661.

Ghiglione, M. C., Suarez, F., Ambrosio, A., Da Poian, G., Cristallini, E. O., Pizzio, M. F., & Reinoso, R. M. (2009). Structure and evolution of the Austral Basin fold-thrust belt, southern Patagonian Andes. *Revista de la Asociación Geológica Argentina*, *65*(1), 215-226.

Glasser, N., & Jansson, K. (2008). The glacial map of southern South America. *Journal of Maps*, *4*(1), 175-196.

Global Volcanism Program, 2023. [Database] Volcanoes of the World (v. 5.0.1; 19 Dec 2022). Distributed by Smithsonian Institution, compiled by Venzke, E. https://doi.org/10.5479/si.GVP.VOTW5-2022.5.0

Glodny, J., Gräfe, K., Echtler, H., & Rosenau, M. (2008). Mesozoic to Quaternary continental margin dynamics in South-Central Chile (36–42 S): the apatite and zircon fission track perspective. *International Journal of Earth Sciences*, *97*(6), 1271-1291.

Glotzbach, C., van der Beek, P. A., & Spiegel, C. (2011). Episodic exhumation and relief growth in the Mont Blanc massif, Western Alps from numerical modeling of thermochronology data. *Earth and Planetary Science Letters*, *304*(3-4), 417-430.

Gorring, M. L., Kay, S. M., Zeitler, P. K., Ramos, V. A., Rubiolo, D., Fernandez, M. I., & Panza, J. L. (1997). Neogene Patagonian plateau lavas: continental magmas associated with ridge collision at the Chile Triple Junction. *Tectonics*, *16*(1), 1-17.

Guenthner, W. R., Barbeau Jr, D. L., Reiners, P. W., & Thomson, S. N. (2010). Slab window migration and terrane accretion preserved by low-temperature thermochronology of a magmatic arc, northern Antarctic Peninsula. *Geochemistry, Geophysics, Geosystems,* 11(3).

Guenthner, W. R., Reiners, P. W., Ketcham, R. A., Nasdala, L., & Giester, G. (2013). Helium diffusion in natural zircon: Radiation damage, anisotropy, and the interpretation of zircon (U-Th)/He thermochronology. *American Journal of Science*, *313*(3), 145-198.

Guillaume, B., Gautheron, C., Simon-Labric, T., Martinod, J., Roddaz, M., & Douville, E. (2013). Dynamic topography control on Patagonian relief evolution as inferred from low temperature thermochronology. *Earth and Planetary Science Letters*, *364*, 157-167.

Guillaume, B., Martinod, J., Husson, L., Roddaz, M., & Riquelme, R. (2009). Neogene uplift of central eastern Patagonia: dynamic response to active spreading ridge subduction?. *Tectonics*, *28*(2).

Guillaume, B., Moroni, M., Funiciello, F., Martinod, J., & Faccenna, C. (2010). Mantle flow and dynamic topography associated with slab window opening: Insights from laboratory models. *Tectonophysics*, *496*(1-4), 83-98.

Guivel, C., Morata, D., Pelleter, E., Espinoza, F., Maury, R. C., Lagabrielle, Y., Polvé, M., Bellon, H., Cotten, J., Benoit, M., Suárez, M., & de La Cruz, R. (2006). Miocene to Late Quaternary Patagonian basalts (46–47 S): geochronometric and geochemical evidence for slab tearing due to active spreading ridge subduction. *Journal of Volcanology and Geothermal Research*, *149*(3-4), 346-370.

Haeuselmann, P., Granger, D. E., Jeannin, P. Y., & Lauritzen, S. E. (2007). Abrupt glacial valley incision at 0.8 Ma dated from cave deposits in Switzerland. Geology, 35(2), 143-146.

Haschke, M., Sobel, E. R., Blisniuk, P., Strecker, M. R., & Warkus, F. (2006). Continental response to active ridge subduction. *Geophysical research letters*, *33*(15).

Hayes, G. P., Moore, G. L., Portner, D. E., Hearne, M., Flamme, H., Furtney, M., & Smoczyk, G. M. (2018). Slab2, a comprehensive subduction zone geometry model. *Science*, *362*(6410), 58-61.

Hein, A. S., Dunai, T. J., Hulton, N. R., & Xu, S. (2011). Exposure dating outwash gravels to determine the age of the greatest Patagonian glaciations. *Geology*, *39*(2), 103-106.

Herman, F., & Brandon, M. (2015). Mid-latitude glacial erosion hotspot related to equatorial shifts in southern Westerlies. *Geology*, *43*(11), 987-990.

Herman, F., & Champagnac, J. D. (2016). Plio-Pleistocene increase of erosion rates in mountain belts in response to climate change. *Terra Nova*, *28*(1), 2-10.

Herman, F., Beaud, F., Champagnac, J. D., Lemieux, J. M., & Sternai, P. (2011). Glacial hydrology and erosion patterns: a mechanism for carving glacial valleys. *Earth and Planetary Science Letters*, *310*(3-4), 498-508.

Herman, F., Braun, J., Deal, E., & Prasicek, G. (2018). The response time of glacial erosion. *Journal of Geophysical Research: Earth Surface*, *123*(4), 801-817.

Herman, F., Seward, D., Valla, P. G., Carter, A., Kohn, B., Willett, S. D., & Ehlers, T. A. (2013). Worldwide acceleration of mountain erosion under a cooling climate. *Nature*, *504*(7480), 423-426.

Herve, F., Pankhurst, R. J., Fanning, C. M., Calderón, M., & Yaxley, G. M. (2007). The South Patagonian batholith: 150 my of granite magmatism on a plate margin. *Lithos*, *97*(3-4), 373-394.

Heuret, A., & Lallemand, S. (2005). Plate motions, slab dynamics and back-arc deformation. *Physics of the Earth and Planetary Interiors*, *149*(1-2), 31-51.

House, M. A., Kohn, B. P., Farley, K. A., & Raza, A. (2002). Evaluating thermal history models for the Otway Basin, southeastern Australia, using (U-Th)/He and fission-track data from borehole apatites. *Tectonophysics*, *349*(1-4), 277-295.

Kaplan, M. R., Ackert Jr, R. P., Singer, B. S., Douglass, D. C., & Kurz, M. D. (2004). Cosmogenic nuclide chronology of millennial-scale glacial advances during O-isotope stage 2 in Patagonia. *Geological Society of America Bulletin*, *116*(3-4), 308-321.

Kaplan, M. R., Hein, A. S., Hubbard, A., & Lax, S. M. (2009). Can glacial erosion limit the extent of glaciation?. *Geomorphology*, *103*(2), 172-179.

Ketcham, R. A., Guenthner, W. R., & Reiners, P. W. (2013). Geometric analysis of radiation damage connectivity in zircon, and its implications for helium diffusion. *American Mineralogist*, *98*(2-3), 350-360.

Klepeis, K., Betka, P., Clarke, G., Fanning, M., Hervé, F., Rojas, L., Mpodozis, C, & Thomson, S. (2010). Continental underthrusting and obduction during the Cretaceous closure of the Rocas Verdes rift basin, Cordillera Darwin, Patagonian Andes. *Tectonics*, *29*(3).

Kohn, B., Chung, L., & Gleadow, A. (2019). Fission-track analysis: Field collection, Sample preparation and Data Acquisition. In Malusà, M. G., and Fitzgerald, P., eds. *Fission-Track Thermochronology and its Application to Geology*. Springer, Cham, Switzerland, p. 25-48. http://www.springer.com/series/15201

Koppes, M. N., & Montgomery, D. R. (2009). The relative efficacy of fluvial and glacial erosion over modern to orogenic timescales. *Nature Geoscience*, *2*(9), 644-647.

Kraemer, P. E. (2003). Orogenic shortening and the origin of the Patagonian orocline (56 S. Lat). *Journal of South American Earth Sciences*, *15*(7), 731-748.

Lagabrielle, Y., Goddéris, Y., Donnadieu, Y., Malavieille, J., & Suarez, M. (2009). The tectonic history of Drake Passage and its possible impacts on global climate. *Earth and Planetary Science Letters*, *279*(3-4), 197-211.

Lagabrielle, Y., Scalabrino, B., Suarez, M., & Ritz, J. F. (2010). Mio-Pliocene glaciations of Central Patagonia: New evidence and tectonic implications. *Andean Geology*, *37*(2), 276-299.

Lagabrielle, Y., Suárez, M., Malavieille, J., Morata, D., Espinoza, F., Maury, R. C., Scalabrino, B., Barbero, L., Cruz, R., Rossello, E., & Bellon, H. (2007). Pliocene extensional tectonics in the Eastern Central Patagonian Cordillera: geochronological constraints and new field evidence. *Terra Nova*, *19*(6), 413-424.

Lagabrielle, Y., Suárez, M., Rossello, E. A., Hérail, G., Martinod, J., Régnier, M., & de la Cruz, R. (2004). Neogene to Quaternary tectonic evolution of the Patagonian Andes at the latitude of the Chile Triple Junction. *Tectonophysics*, *385*(1-4), 211-241.

Lallemand, S. E., Malavieille, J., & Calassou, S. (1992). Effects of oceanic ridge subduction on accretionary wedges: Experimental modeling and marine observations. *Tectonics*, *11*(6), 1301-1313.

Leuthold, J., Müntener, O., Baumgartner, L. P., Putlitz, B., Ovtcharova, M., & Schaltegger, U. (2012). Time resolved construction of a bimodal laccolith (Torres del Paine, Patagonia). *Earth and Planetary Science Letters*, *325*, 85-92.

Lisiecki, L. E. (2010). A benthic δ13C-based proxy for atmospheric pCO2 over the last 1.5 Myr. *Geophysical Research Letters*, *37*(21).

Lisiecki, L. E., & Raymo, M. E. (2007). Plio–Pleistocene climate evolution: trends and transitions in glacial cycle dynamics. *Quaternary Science Reviews*, *26*(1-2), 56-69.

Malkowski, M. A., Sharman, G. R., Graham, S. A., & Fildani, A. (2017). Characterisation and diachronous initiation of coarse clastic deposition in the Magallanes–Austral foreland basin, Patagonian Andes. *Basin Research*, *29*, 298-326.

Maloney, K. T., Clarke, G. L., Klepeis, K. A., & Quevedo, L. (2013). The Late Jurassic to present evolution of the Andean margin: Drivers and the geological record. *Tectonics*, *32*(5), 1049-1065.

Mercer, J. H., & Sutter, J. F. (1982). Late Miocene—earliest Pliocene glaciation in southern Argentina: implications for global ice-sheet history. *Palaeogeography, Palaeoclimatology, Palaeoecology*, *38*(3-4), 185-206.

Molnar, P. (2004). Late Cenozoic increase in accumulation rates of terrestrial sediment: How might climate change have affected erosion rates?. *Annu. Rev. Earth Planet. Sci.*, *32*, 67-89.

Molnar, P. (2004). Late Cenozoic increase in accumulation rates of terrestrial sediment: How might climate change have affected erosion rates?. *Annu. Rev. Earth Planet. Sci.*, *32*, 67-89.

Molnar, P., England, P., & Martinod, J. (1993). Mantle dynamics, uplift of the Tibetan Plateau, and the Indian monsoon. *Reviews of Geophysics*, *31*(4), 357-396.

Montgomery, D. R., Balco, G., & Willett, S. D. (2001). Climate, tectonics, and the morphology of the Andes. *Geology*, *29*(7), 579-582.

Muller, V. A., Calderón, M., Fosdick, J. C., Ghiglione, M. C., Cury, L. F., Massonne, H. J., Fannin, C. M., Warren, C., Ramírez de Arellano, C. & Sternai, P. (2021). The closure of the Rocas Verdes Basin and early tectono-metamorphic evolution of the Magallanes Fold-and-Thrust Belt, southern Patagonian Andes (52–54° S). *Tectonophysics*, *798*, 228686.

Nasdala, L., Wenzel, M., Vavra, G., Irmer, G. and Kober, B. (2001) Metamictisation of natural zircon: accumulation versus thermal annealing of radioactivity-induced damage. *Contrib. Min. Petrol*. 141, 125-144.

Pedersen, V. K., & Egholm, D. L. (2013). Glaciations in response to climate variations preconditioned by evolving topography. *Nature*, *493*(7431), 206-210.

Peizhen, Z., Molnar, P., & Downs, W. R. (2001). Increased sedimentation rates and grain sizes 2–4 Myr ago due to the influence of climate change on erosion rates. *Nature*, *410*(6831), 891-897.

Putlitz, B., Baumgartner, L.P., Oberhaensli, R., Diamond, L., Altenberger, U. (2001). The Torres del Paine Laccolith (Chile); intrusion and metamorphism. XI Goldschmidt Conference, Abstract No. 3534. Hot Springs, United States.

Rabassa, J. (2008). Late cenozoic glaciations in Patagonia and Tierra del Fuego. *Developments in quaternary sciences*, *11*, 151-204.

Rabassa, J., Coronato, A. M., & Salemme, M. (2005). Chronology of the Late Cenozoic Patagonian glaciations and their correlation with biostratigraphic units of the Pampean region (Argentina). *Journal of South American Earth Sciences*, *20*(1-2), 81-103.

Rabassa, J., Coronato, A., & Martinez, O. (2011). Late Cenozoic glaciations in Patagonia and Tierra del Fuego: an updated review. *Biological Journal of the Linnean Society*, *103*(2), 316-335.

Ramírez de Arellano, C. (2011). *Petrology and chemistry of the Chaltén Plutonic Complex and implications on the magmatic and tectonic evolution of the Southernmost Andes (Patagonia) during the Miocene* (Doctoral dissertation, Université de Lausanne, Faculté des géosciences et de l'environnement).

Ramírez de Arellano, C., Putlitz, B., Müntener, O., & Ovtcharova, M. (2012). High precision U/Pb zircon dating of the Chaltén Plutonic Complex (Cerro Fitz Roy, Patagonia) and its relationship to arc migration in the southernmost Andes. *Tectonics*, *31*(4).

Ramos, V. A. (2005). Seismic ridge subduction and topography: Foreland deformation in the Patagonian Andes. *Tectonophysics*, *399*(1-4), 73-86.

Ramos, V. A., & Kay, S. M. (1992). Southern Patagonian plateau basalts and deformation: backarc testimony of ridge collisions. *Tectonophysics*, *205*(1-3), 261-282.

Recanati, A., Gautheron, C., Barbarand, J., Missenard, Y., Pinna-Jamme, R., Tassan-Got, L., Carter, A., Douville, E., Bordier, L., Pagel, M., & Gallagher, K. (2017). Helium trapping in apatite damage: Insights from (U-Th-Sm)/He dating of different granitoid lithologies. *Chemical Geology*, *470*, 116-131.

Reiners, P. W. (2005). Zircon (U-Th)/He thermochronometry. *Reviews in Mineralogy and Geochemistry*, *58*(1), 151-179.

Reiners, P. W., & Brandon, M. T. (2006). Using thermochronology to understand orogenic erosion. *Annual Review of Earth and Planetary Sciences*, *34*(1), 419-466.

Reiners, P. W., Spell, T. L., Nicolescu, S., & Zanetti, K. A. (2004). Zircon (U-Th)/He thermochronometry: He diffusion and comparisons with 40Ar/39Ar dating. *Geochimica et cosmochimica acta*, *68*(8), 1857-1887.

Reiners, P.W. (2005) Zircon (U-Th)/He thermochronometry, in: Reiners, P.W., Ehlers, T.A. (Eds.), *Thermochronology, Reviews in Mineralogy and Geochemistry*, pp. 151-179.

Reiners, P.W. & Farley, K.A. (2001) Influence of crystal size on apatite (U+Th)/He thermochronology: an example from the Bighorn Mountains, Wyoming. *Earth Planet. Sci. Lett.* 188, 413-420.

Ronda, G., Ghiglione, M. C., Martinod, J., Barberón, V., Ramos, M. E., Coutand, I., Grujic, D., & Kislitsyn, R. (2022). Early Cretaceous to Cenozoic Growth of the Patagonian Andes as Revealed by Low‐Temperature Thermochronology. *Tectonics*, *41*(10), e2021TC007113.

Ruddiman, W. F., Raymo, M. E., Prell, W. L., & Kutzbach, J. E. (1997). The uplift-climate connection: a synthesis. In *Tectonic uplift and climate change* (pp. 471-515). Springer, Boston, MA.

Salze, M., Martinod, J., Guillaume, B., Kermarrec, J. J., Ghiglione, M. C., & Sue, C. (2018). Trench-parallel spreading ridge subduction and its consequences for the geological evolution of the overriding plate: Insights from analogue models and comparison with the Neogene subduction beneath Patagonia. *Tectonophysics*, *737*, 27-39.

Scalabrino, B., Lagabrielle, Y., Malavieille, J., Dominguez, S., Melnick, D., Espinoza, F., Suarez, M, & Rossello, E. (2010). A morphotectonic analysis of central Patagonian Cordillera: Negative inversion of the Andean belt over a buried spreading center?. *Tectonics*, *29*(2).

Schildgen, T. F., Balco, G., & Shuster, D. L. (2010). Canyon incision and knickpoint propagation recorded by apatite 4He/3He thermochronometry. *Earth and Planetary Science Letters*, *293*(3-4), 377-387.

Shuster, D. L., & Farley, K. A. (2004). 4He/3He thermochronometry. *Earth and Planetary Science Letters*, *217*(1-2), 1-17.

Shuster, D. L., Cuffey, K. M., Sanders, J. W., & Balco, G. (2011). Thermochronometry reveals headward propagation of erosion in an alpine landscape. *Science*, *332*(6025), 84-88.

Shuster, D. L., Ehlers, T. A., Rusmoren, M. E., & Farley, K. A. (2005). Rapid glacial erosion at 1.8 Ma revealed by 4He/3He thermochronometry. *Science*, *310*(5754), 1668-1670.

Shuster, D. L., Flowers, R. M., & Farley, K. A. (2006). The influence of natural radiation damage on helium diffusion kinetics in apatite. *Earth and Planetary Science Letters*, *249*(3-4), 148-161.

Singer, B. S., Ackert Jr, R. P., & Guillou, H. (2004). 40Ar/39Ar and K-Ar chronology of Pleistocene glaciations in Patagonia. *Geological Society of America Bulletin*, *116*(3-4), 434-450.

Spotila, J. A. (2005). Applications of low-temperature thermochronometry to quantification of recent exhumation in mountain belts. *Reviews in Mineralogy and Geochemistry*, *58*(1), 449-466.

Stern, C. R., Futa, K., & Muehlenbachs, K. A. R. L. I. S. (1984). Isotope and trace element data for orogenic andesites from the Austral Andes. In *Andean magmatism* (pp. 31-46). Birkhäuser Boston.

Sternai, P., Avouac, J. P., Jolivet, L., Faccenna, C., Gerya, T., Becker, T. W., & Menant, A. (2016). On the influence of the asthenospheric flow on the tectonics and topography at a collision-subduction transition zones: Comparison with the eastern Tibetan margin. *Journal of Geodynamics*, *100*, 184-197.

Sternai, P., Herman, F., Fox, M. R., & Castelltort, S. (2011). Hypsometric analysis to identify spatially variable glacial erosion. *Journal of Geophysical Research: Earth Surface*, *116*(F3).

Sternai, P., Herman, F., Valla, P. G., & Champagnac, J. D. (2013). Spatial and temporal variations of glacial erosion in the Rhône valley (Swiss Alps): Insights from numerical modeling. *Earth and Planetary Science Letters*, *368*, 119-131.

Sternai, P., Sue, C., Husson, L., Serpelloni, E., Becker, T. W., Willett, S. D., Faccenna, C., Di Giulio, A., Spada, G., Jolivet, L., Valla, P., Petit, C. Nocquet, J.-M, Walpersdorf, A., &

Castelltort, S. (2019). Present-day uplift of the European Alps: Evaluating mechanisms and models of their relative contributions. *Earth-Science Reviews*, *190*, 589-604.

Stevens Goddard, A. L., & Fosdick, J. C. (2019). Multichronometer thermochronologic modeling of migrating spreading ridge subduction in southern Patagonia. *Geology*, *47*(6), 555-558.

Suárez, M., De La Cruz, R., & Bell, C. M. (2000). Timing and origin of deformation along the Patagonian fold and thrust belt. *Geological Magazine*, *137*(4), 345-353.

Thomson, S. N., Brandon, M. T., Tomkin, J. H., Reiners, P. W., Vásquez, C., & Wilson, N. J. (2010). Glaciation as a destructive and constructive control on mountain building. *Nature*, *467*(7313), 313-317.

Thomson, S. N., Hervé, F., & Stöckhert, B. (2001). Mesozoic-Cenozoic denudation history of the Patagonian Andes (southern Chile) and its correlation to different subduction processes. *Tectonics*, *20*(5), 693-711.

Thorndycraft, V. R., Bendle, J. M., Benito, G., Davies, B. J., Sancho, C., Palmer, A. P., .Fabel, D., Medialdea, A., & Martin, J. R. (2019). Glacial lake evolution and Atlantic-Pacific drainage reversals during deglaciation of the Patagonian Ice Sheet. *Quaternary Science Reviews*, *203*, 102-127.

Tomkin, J. H., & Roe, G. H. (2007). Climate and tectonic controls on glaciated critical-taper orogens. *Earth and Planetary Science Letters*, *262*(3-4), 385-397.

Valla, P. G., Shuster, D. L., & Van Der Beek, P. A. (2011). Significant increase in relief of the European Alps during mid-Pleistocene glaciations. *Nature geoscience*, *4*(10), 688-692.

Wagner, G. A., & Reimer, G. M. (1972). Fission track tectonics: the tectonic interpretation of fission track apatite ages. *Earth and Planetary Science Letters*, *14*(2), 263-268.

Wagner, G.A. (1979) Correction and interpretation of fission track ages. In: Jäger E, Hunziker JC (eds) *Lectures in isotope geology*. Springer, Berlin Heidelberg New York, pp 170–177

Whipple, K. X. (2009). The influence of climate on the tectonic evolution of mountain belts. *Nature geoscience*, *2*(2), 97-104.

Whipple, K. X., & Tucker, G. E. (1999). Dynamics of the stream-power river incision model: Implications for height limits of mountain ranges, landscape response timescales, and research needs. *Journal of Geophysical Research: Solid Earth*, *104*(B8), 17661-17674.

Willett, C. D., Ma, K. F., Brandon, M. T., Hourigan, J. K., Christeleit, E. C., & Shuster, D. L. (2020). Transient glacial incision in the Patagonian Andes from~ 6 Ma to present. *Science advances*, *6*(7), eaay1641.

Willett, S. D. (1999). Orogeny and orography: The effects of erosion on the structure of mountain belts. *Journal of Geophysical Research: Solid Earth*, *104*(B12), 28957-28981.

Willett, S. D., Slingerland, R., & Hovius, N. (2001). Uplift, shortening, and steady state topography in active mountain belts. *American journal of Science*, *301*(4-5), 455-485.

Zachos, J., Pagani, M., Sloan, L., Thomas, E., & Billups, K. (2001). Trends, rhythms, and aberrations in global climate 65 Ma to present. *Science*, *292*(5517), 686-693.

Zeitler, P. K., Herczeg, A. L., McDougall, I., & Honda, M. (1987). U-Th-He dating of apatite: A potential thermochronometer. *Geochimica et Cosmochimica Acta*, *51*(10), 2865-2868.

Table 1. Zircon (U-Th)/He (ZHe) data for Fitz Roy (FzR) samples.

Sample N°	Latitude/ Longitude (°S/°W)	Elevation (m)	U (ppm)	Th (ppm)	Sm (ppm)	^{4}He (nmol/g)	Rs (μm)	F_T	Raw age (Ma)	Raw error (Ma)	Corrected Age (Ma)	1σ error (Ma)
FZR3-1			205.8	91.5	6.0	7.9	54.35	0.78	6.4	0.04	8.2	0.1
FZR3-2			284.3	100.8	2.5	11.1	56.52	0.79	6.7	0.04	8.5	0.1
FZR3-3			506.7	156.9	3.4	18.8	53.10	0.78	6.4	0.04	8.2	0.1
FZR3-4			516.9	138.7	2.5	19.7	53.24	0.78	6.6	0.04	8.5	0.1
FZR3-5			513.1	198.4	2.6	21.0	51.87	0.77	6.7	0.04	8.7	0.1
FZR3	**49.2566/ 49.2566/**	**2070**									**8.4 ±0.2**	
FZR4-1			371.3	140.9	3.5	13.7	47.51	0.76	6.3	0.04	8.3	0.1
FZR4-3			309.6	109.3	2.5	11.6	52.78	0.78	6.4	0.04	8.3	0.1
FZR4-4			1128.8	326.6	3.9	34.6	45.21	0.75	5.3	0.03	7.1	0.4
FZR4-5			715.6	234.1	2.9	23.7	52.90	0.78	5.7	0.03	7.3	0.4
FZR4	**49.2550/ 73.0281**	**1955**									**7.7 ±0.6**	
FZR5-1			904.2	321.4	7.4	35.6	52.99	0.78	6.7	0.04	8.7	0.5
FZR5-2			271.4	96.8	3.1	11.4	46.23	0.75	7.1	0.04	9.6	0.6
FZR5-3			412.4	310.9	5.7	12.0	45.33	0.74	4.6	0.03	6.2	0.4
FZR5-4			527.9	246.5	6.5	22.5	43.24	0.73	7.1	0.04	9.7	0.6
FZR5-5			529.4	268.6	5.2	14.3	43.28	0.73	4.5	0.03	6.1	0.4
FZR5	**49.2540/ 73.0311**	**1758**									**8.0 ±1.8**	
FZR6-1			1157.2	380.0	8.4	66.4	49.97	0.77	9.9	0.06	12.9	0.8
FZR6-2			1221.7	476.3	9.3	62.1	45.48	0.75	8.6	0.05	11.6	0.7
FZR6-3			1021.0	290.1	4.2	41.4	43.47	0.74	7.1	0.04	9.6	0.6
FZR6-4			403.0	141.7	2.8	11.6	44.43	0.74	4.9	0.03	6.7	0.4
FZR6	**49.2487/ 73.0327**	**1569**									**10.2 ±2.7**	

Notes. Ft = age correction factor (Farley et al., 1996). Bold numbers are mean ages calculated from the single-crystal replicates; 1σ error for mean ages is standard deviation of replicate ages. Analytical uncertainties are around 6% of the corrected age.

Table 2. Apatite (U-Th)/He (AHe) data for Fitz Roy (FzR) samples.

Sample N°	Latitude/ Longitude (°S/°W)	Elevation (m)	U (ppm)	Th (ppm)	Sm (ppm)	^{4}He (nmol/g)	Rs (μm)	F_t	Raw age (Ma)	Raw error (Ma)	Corrected Age (Ma)	1σ error (Ma)
FZR10-M			13.3	38.2	277.3	0.7	43.5	0.73	5.5	0.9	7.5	0.6
FZR10-N			53.3	168.0	436.1	3.6	42.2	0.73	7.1	1.2	9.7	0.8
FZR10	**49.2543/ 73.0319**	**1780**									**8.6±1.6**	
FZR11-A			3.5	12.0	103.0	0.2	55.4	0.80	4.3	1.0	5.4	0.4
FZR11-D			8.0	19.9	170.5	0.5	51.1	0.77	6.9	0.7	8.9	0.7
FZR11-E			23.5	38.6	122.4	0.8	60.7	0.80	4.5	0.7	5.7	0.5
FZR11-L			14.4	46.4	344.1	0.6	40.0	0.73	3.8	0.0	5.1	0.4
FZR11	**49.2538/ 73.0346**	**1840**									**6.2±1.4**	
FZR12-E			7.3	20.6	136.3	0.4	57.1	0.78	5.2	0.8	6.7	0.5
FZR12-M			23.6	68.0	381.9	1.3	41.8	0.71	5.9	1.0	8.3	0.7
FZR12-N			15.3	45.8	250.0	0.9	47.0	0.76	6.2	1.1	8.1	0.7
FZR12	**49.2493/ 73.0364**	**1765**									**7.7±0.9**	
FZR13-B			26.9	46.2	140.1	0.9	56.3	0.77	4.7	0.0	6.0	0.1
FZR13-F			7.9	22.8	83.5	0.4	77.0	0.84	5.0	0.0	6.0	0.1
FZR13-L			71.3	135.8	461.4	2.5	41.3	0.69	4.3	0.7	6.3	0.3
FZR13	**49.2553/ 73.0473**	**1410**									**6.1±0.2**	
FZR14-A			10.0	17.4	105.9	0.4	66.3	0.81	5.6	0.2	6.9	0.1
FZR14-D			11.1	30.5	186.5	0.6	54.2	0.74	6.0	0.2	8.1	0.1
FZR14-E			10.5	29.4	183.3	0.6	58.0	0.75	5.6	0.2	7.5	0.1
FZR14-F			6.7	19.5	76.1	0.4	79.4	0.85	6.3	0.2	7.4	0.1
FZR14-G			9.8	24.9	100.2	0.6	74.9	0.84	6.3	0.2	7.5	0.1
FZR14	**49.2586/ 73.0493**	**1530**									**7.5±0.4**	
FZR15-A			28.3	72.1	150.8	1.1	64.5	0.78	4.6	0.0	5.8	0.1
FZR15-D			27.3	78.1	130.8	1.2	70.5	0.80	4.7	0.0	5.9	0.1

FZR15-F			36.3	106.9	214.3	1.6	55.7	0.75	4.8	0.0	6.4	0.1
FZR15	**49.2715/ 73.0568**	**1910**									**6.0±0.3**	
FZR16-A			13.7	40.9	131.7	0.4	57.3	0.78	3.0	0.0	3.9	0.1
FZR16-C			14.2	40.2	109.1	0.3	63.4	0.82	2.6	0.0	3.1	0.1
FZR16-E			12.2	38.5	68.9	0.4	78.0	0.83	3.8	0.0	4.6	0.1
FZR16	**49.2654/ 73.0586**	**1710**									**3.9±0.7**	

Notes. Ft = age correction factor (Farley et al., 1996). Bold numbers are mean ages calculated from the single-crystal replicates; 1σ error for mean ages is standard deviation of replicate ages. Analytical uncertainties are <1, ~3 and ~2% for respectively U, Th and Sm measurements; and <1% for ^{4}He measurements.

Table 3a. Apatite (U-Th)/He (AHe) data for Torres del Paine (TdP) samples, Central sector.

Sample N°	Latitude/ Longitude (°S/°W)	Elevation (m)	U (ppm)	Th (ppm)	Sm (ppm)	^{4}He (nmol/g)	Rs (μm)	F_t	Raw age (Ma)	Raw error (Ma)	Corrected Age (Ma)	1σ error (Ma)
04-JM-66ap1			8.2	10.1	442.4	0.5	53.6	0.73	8.6	0.3	11.7	0.4
04-JM-66ap2			5.1	11.2	291.3	0.3	54.8	0.73	6.7	0.2	9.2	0.2
04-JM-66ap3			8.8	13.3	397.6	0.5	39.8	0.64	7.6	0.3	11.9	0.4
04-JM-66ap4			32.4	40.9	575.7	2.2	55.5	0.74	9.6	0.2	13.1	0.3
04-JM-66	**50.97541/ 73.02521**	**1802**									**11.5±1.6**	
04-JM-67ap1			7.5	16.9	290.2	0.4	61.4	0.76	6.1	0.1	8.1	0.1
04-JM-67ap2			54.2	75.2	1128.1	3.4	59.0	0.75	8.2	0.1	10.9	0.2
04-JM-67ap3			8.9	21.1	442.6	0.6	77.4	0.81	7.5	0.1	9.3	0.1
04-JM-67ap4			53.9	67.3	996.1	2.0	56.3	074	5.2	0.1	7.1	0.1
04-JM-67ap5			14.3	30.9	647.5	0.8	42.1	0.65	6.5	0.2	10.0	0.4
04-JM-67	**50.97492/ 73.02651**	**1731**									**9.1±1.5**	
04-JM-68ap1			4.2	11.6	162.0	0.3	76.7	0.80	7.3	0.2	9.1	0.3
04-JM-68ap2			8.4	15.4	309.2	0.3	54.3	0.73	5.0	0.2	6.8	0.3
04_JM-68	**50.97405/ 73.02843**	**1619**									**8.0±1.6**	
04-JM-71ap1			36.1	89.2	701.2	1.4	72.0	0.81	4.6	0.1	5.7	0.1
04-JM-71ap2			15.1	25.1	508.5	0.8	70.6	0.79	6.7	0.1	8.5	0.1
04-JM-71ap4			19.8	26.2	579.9	0.8	59.0	0.75	5.8	0.2	7.7	0.2
04-JM-71	**50.97342/ 73.03557**	**1310**									**7.3±1.5**	
04-JM-76ap1			15.2	21.6	466.1	0.5	46.2	0.69	5.1	0.3	7.3	0.4
04-JM-76ap2			21.1	41.2	503.4	0.7	41.1	0.65	4.0	0.2	6.1	0.4
04-JM-76ap3			41.2	42.2	539.9	1.2	46.8	0.69	4.4	0.1	6.4	0.2
04-JM-76	**50.97449/ 73.03936**	**1189**									**6.6±0.6**	
04-JM-87ap1			11.1	31.8	448.1	0.4	42.5	0.66	4.1	0.3	6.2	0.4
04-JM-87ap2			21.9	50.8	291.5	1.1	98.3	0.84	6.0	0.1	7.1	0.1

04-JM-87ap3			17.9	25.5	588.6	0.6	58.1	0.75	4.4	0.1	5.9	0.1
04-JM-87	**50.97638/ 73.04372**	**1042**									**6.4±0.6**	
04-JM-90ap1			28.0	22.8	254.3	0.7	50.5	0.71	3.8	0.1	5.3	0.2
04-JM-90ap2			12.7	28.5	352.8	0.6	66.7	0.77	5.9	0.2	7.7	0.2
04-JM-90ap3			22.3	29.9	312.2	0.8	63.7	0.77	5.2	0.2	6.8	0.2
04-JM-90	**50.98166/ 73.05553**	**758**									**6.6±1.2**	
08-JL-385ap1			18.6	64.7	185.9	0.7	46.4	0.68	3.8	0.1	5.7	0.1
08-JL-385ap2			2.2	0.9	0.2	0.1	47.1	0.70	3.8	0.3	5.5	0.5
08-JL-385ap3			11.2	33.6	270.3	0.5	44.3	0.67	5.2	0.2	7.7	0.2
08-JL-385ap4			26.7	60.4	397.6	0.7	38.4	0.62	3.3	0.1	5.3	0.2
08-JL-385ap5			44.8	128.8	299.4	2.2	48.6	0.69	5.3	0.1	7.6	0.1
08-JL-385	**50.97669/ 73.10013**	**1175**									**6.4±1.2**	
07-JL-160ap2			5.1	23.4	208.1	0.3	57.1	0.73	4.6	0.1	6.2	0.1
07-JL-160ap3			5.3	21.8	145.7	0.2	57.7	0.74	4.0	0.1	5.4	0.1
07-JL-160ap4			9.1	30.8	181.9	0.4	51.1	0.71	4.4	0.1	6.2	0.1
07-JL-160	**50.97677/ 73.10036**	**1200**									**6.0±0.4**	
07-JL-165ap4			20.8	40.3	222.7	0.7	49.2	0.70	4.5	0.1	6.4	0.1
07-JL-165ap4			16.7	54.4	250.3	0.5	47.9	0.69	3.1	0.1	4.4	0.1
07-JL-165ap4			42.7	93.2	317.6	1.7	50.6	0.71	5.0	0.1	7.1	0.1
07-JL-165ap4			21.3	43.4	285.7	0.6	42.0	0.65	3.5	0.1	5.4	0.2
07-JL-165	**50.97718/ 73.10087**	**1275**									**5.8±1.2**	
04-JM-49ap1			10.5	42.3	416.6	0.5	57.2	0.74	4.7	0.1	6.4	0.1
04-JM-49ap2			9.5	26.6	348.4	0.4	60.0	0.75	4.2	0.1	5.6	0.1
04-JM-49ap3			8.2	24.7	330.6	0.3	46.1	0.68	3.3	0.1	4.9	0.1
04-JM-49ap4			8.4	24.2	285.5	0.5	64.0	0.77	5.9	0.1	7.6	0.1
04-JM-49	**51.04051/ 73.08473**	**785**									**6.1±1.2**	
04-JM-30ap1			9.1	12.8	501.3	0.5	68.8	0.79	7.2	0.0	9.18	0.4
04-JM-30ap2			15.8	38.0	671.1	0.8	51.2	0.71	6.0	0.2	8.46	0.2

04-JM-30	**50.94709/ 72.99015**	**1830**									**8.8±0.5**	
04-JM-23ap1			6.2	14.9	317.0	0.3	63.9	0.77	5.2	0.2	6.77	0.2
04-JM-23ap2			6.7	12.9	352.7	0.3	40.8	0.65	4.2	0.5	6.53	0.8
04-JM-23	**50.94713/ 72.99902**	**1461**									**6.7±0.2**	
13-TP-26-a			16.8	90.4	60.5	0.5	56.4	0.74	2.3	0.1	3.08	0.1
13-TP-26-z-BR			10.6	40.0	53.3	0.5	63.3	0.77	4.1	0.1	5.37	0.1
13-TP-26-y-BR			9.8	34.3	46.4	0.3	63.6	0.77	3.1	0.1	4.11	0.1
13-TP-26-x			11.3	45.6	51.8	0.4	59.2	0.75	3.2	0.1	4.22	0.1
13-TP-26	**50.9728/ 72.8839**	**206**									**4.2±0.9**	
CH15-19	**51.01057/ 72.94342**	**372**	0.2	3.3	23.6	0.1	84.8	0.82	3.7	0.4	**4.4±0.5**	
CH15-TP21_x			4.9	30.1	51.4	0.2	69.6	0.78	2.7	0.1	3.42	0.1
CH15-TP21_y			11.3	13.1	34.1	0.2	55.4	0.73	3.0	0.1	4.14	0.1
CH15-TP21_z			3.7	16.7	13.1	0.1	67.1	0.78	3.0	0.1	3.91	0.1
CH15-TP21	**50.98973/ 72.79723**	**268**									**3.8±0.4**	
CH15_TP30_x			1.7	11.3	16.1	0.1	78.9	0.81	5.7	0.1	7.19	0.1
CH15_TP30_y			1.5	11.3	19.5	0.1	66.2	0.77	3.4	0.1	7.01	0.1
CH15_TP30_z			1.1	11.826	12.423	0.097	60.4	0.75	4.5	0.3	6.1	0.4
CH15_TP30	**50.94726/ 72.90560**	**1053**									**6.8±0.6**	

Notes. Ft = age correction factor (Farley et al., 1996). Bold numbers are mean ages calculated from the single-crystal replicates; 1σ error for mean ages is standard deviation of replicate ages. Analytical uncertainties are <1, ~3 and ~2% for respectively U, Th and Sm measurements; and <1% for ^{4}He measurements.

Table 3b. Apatite (U-Th)/He (AHe) data for Torres del Paine (TdP) samples, West sector.

Sample N°	Latitude/ Longitude (°S/°W)	Elevation (m)	U (ppm)	Th (ppm)	Sm (ppm)	^{4}He (nmol/g)	Rs (μm)	F_t	Raw age (Ma)	Raw error (Ma)	Corrected Age (Ma)	1σ error (Ma)
CH15-TP14_x			11.8	86.6	46.4	0.9	77.7	0.81	4.9	0.1	6.2	0.1
CH15-TP14_z			1.6	15.6	23.1	0.1	58.7	0.75	4.3	0.1	5.9	0.1
CH15-TP14	**51.25035/ 73.24379**	**112**									**6.1±0.2**	
CH15-TP15_x			5.0	6.4	21.9	0.2	61.2	0.76	6.0	0.1	7.9	0.1
CH15-TP15_y			3.0	20.9	20.1	0.2	61.4	0.76	5.3	0.1	7.2	0.2
CH15-TP15_z			2.7	18.6	34.1	0.3	48.6	0.70	7.5	0.1	11.0	0.2
CH15-TP15	**50.98633/ 73.21632**	**235**									**8.7±2.0**	
CH15_TP22_x			9.9	7.0	18.1	0.5	60.4	0.75	7.7	0.1	10.3	0.1
CH15_TP22_y			2.9	16.8	14.9	0.2	47.5	0.69	6.1	0.2	9.0	0.4
CH15_TP22_z			0.8	23.3	12.3	0.2	55.8	0.73	7.2	0.6	10.2	0.8
CH15_TP22	**51.00625/ 73.14149**	**746**									**9.8±0.7**	

Notes. Ft = age correction factor (Farley et al., 1996). Bold numbers are mean ages calculated from the single-crystal replicates; 1σ error for mean ages is standard deviation of replicate ages. Analytical uncertainties are <1, ~3 and ~2% for respectively U, Th and Sm measurements; and <1% for ^{4}He measurements.

Table 3c. Apatite (U-Th)/He (AHe) data for Torres del Paine (TdP) samples, North sector.

Sample N°	Latitude/ Longitude (°S/°W)	Elevation (m)	U (ppm)	Th (ppm)	Sm (ppm)	^{4}He (nmol/g)	Rs (μm)	F_t	Raw age (Ma)	Raw error (Ma)	Corrected Age (Ma)	1σ error (Ma)
CH15-TP17_y			2.3	15.1	25.2	0.2	72.4	0.79	5.3	0.1	6.3	0.2
CH15_TP17_z			1.8	15.6	36.7	0.2	54.9	0.73	7.5	0.1	6.6	0.2
CH15_TP17	**50.81598/ 73.12218**	**369**									**6.46±0.2**	
CH15_TP26_x			31.3	49.5	53.9	1.8	83.9	0.82	7.8	0.1	9.6	0.1
CH15_TP26_y			34.9	41.4	41.4	1.1	62.0	0.76	4.6	0.1	6.1	0.2
CH15_TP26_z			13.3	23.8	38.6	0.8	69.3	0.78	8.1	0.1	10.4	0.1
CH15_TP26	**50.85859/ 73.12883**	**916**									**8.71±2.27**	

Notes. Ft = age correction factor (Farley et al., 1996). Bold numbers are mean ages calculated from the single-crystal replicates; 1σ error for mean ages is standard deviation of replicate ages. Analytical uncertainties are <1, ~3 and ~2% for respectively U, Th and Sm measurements; and <1% for ^{4}He measurements.